Title

CO2 storage and potential fault instability in the St. Lawrence Lowlands sedimentary basin (Quebec, Canada): Insights from coupled reservoir-geomechanical modeling

Authors

Konstantinovskaya, E
Rutqvist, J
Malo, M

Publication Date

2014-03-01

DOI

10.1016/j.ijggc.2013.12.008

Peer reviewed

CO_2 storage and potential fault instability in the St. Lawrence Lowlands sedimentary basin (Quebec, Canada): insight from coupled reservoir-geomechanical modeling

E. Konstantinovskaya[1*], J. Rutqvist[2], M. Malo[1]

[1] Institut National de la Recherche Scientifique (INRS), 490, de la Couronne, Québec (QC) G1K9A9 Canada; Elena.Konstantinovskaya@ete.inrs.ca; mmalo@ete.inrs.ca

[2] Lawrence Berkeley National Laboratory (LBNL), Berkeley, CA 94720, USA; jrutqvist@lbl.gov

A coupled reservoir-geomechanical (TOUGH-FLAC) modeling is applied for the first time in the St. Lawrence Lowlands region to evaluate the potential shear failure along pre-existing high-angle normal faults and tensile failure in the caprock units (Utica Shale and Lorraine Group) associated with CO_2 injection into the sandstone reservoir (Covey Hill Formation) of the Early Paleozoic sedimentary basin. Field and subsurface data are used to estimate sealing properties of two reservoir-bounding faults (Yamaska and Champlain Faults). The spatial variations in fluid pressure, effective minimum horizontal stress and shear strain are calculated for different injection rates using a simplified 2D geological model of the Becancour area located ~110 km to the SW of Quebec City. The simulation results show that initial fault permeability affects the timing, localization, rate and length of fault shear slip. Contrary to the conventional view, our results suggest that shear failure may start earlier in time in the case of a permeable fault rather than in the case of a sealing fault depending on the site-specific geologic setting. In the simulations, shear slip is nucleated along a 60-m-long fault segment in a thin and brittle caprock unit (Utica Shale) trapped below a thicker and more ductile caprock unit (Lorraine Group), and subsequently progressing up to the surface. In the case of an assumed sealing fault, shear failure occurs later in time and it is localized along a fault segment (300 m) below the caprock units. The presence of the inclined low-permeable Yamaska fault close to the injection well causes asymmetric fluid pressure build-up and lateral migration of CO_2 plume away from the fault that reduces the overall risk of CO_2 leakage along faults. The fluid pressure-induced tensile fracturing occurs only under extremely high injection rates; and it is localized below the caprock units, which remain intact preventing upward CO_2 migration.

1. INTRODUCTION

The changes in fluid pressure and shear stress accumulation may trigger reactivation of faults, which are optimally oriented relative to in-situ stress fields (Davies et al., 2013; Miller et al., 2004; Sibson, 1992; Streit and Cox, 2001). The high fluid injection rates and low permeability of reservoir formation may contribute to the risk of induced seismicity (Berry and Hasegawa, 1979; McClain, 1970). The incidents of fault reactivation and induced earthquakes related to large-volume fluid injection or gas extraction are well known in sites of Snipe Lake and Strachan (Alberta), Wilmington (California), Rangely and Denver (Colorado), midcontinent region of the United States, In Salah (Algeria) (Baranova et al., 1999; Ellsworth, 2013; Healy et al., 1968; Hsieh and Bredehoeft, 1981; Mathieson et al. 2010, 2011; Milne, 1970; Nicol et al., 2011; Raleigh et al., 1976; Shemeta et al., 2012; Suckale, 2010; Wyss and Molnar, 1972).

Even if no harmful induced seismicity has been associated with global carbon capture and storage (CCS) demonstration projects as of February 2011 (Committee, 2012; NETL, 2013), the continuous CO_2 injection at high rates under high pressures for very long periods of time may lead to increase of fluid pressures in storage reservoirs and thus to potential fault reactivation. The CO_2 volume stored in deep saline aquifers in industrial projects to date varies from about 0.7-1 Mt/yr. (e.g. SnØhvit and Sleipner, Norway; In Salah, Algeria; Illinois, U.S.; Quest, Alberta) up to 3-4 Mt/yr. (Gorgon, Western Australia) (GCCSI, 2012). The maximum period of injection time in operating CCS projects to date varies from 17 years in deep saline aquifers (Sleipner, Norway) to 40 years in enhanced oil recovery (EOR) project (Val Verde, Texas) (GCCSI, 2012). The risks of induced seismicity associated with CO_2 storage may be minimized through careful site characterisation and numerical modeling.

The hydromechanical behaviour of faults has been studied to assess the risks of induced seismicity and fluid leakage related to CO_2 storage (Chiaramonte et al., 2008; Hawkes et al., 2005; Lucier et al., 2006; Murphy et al., 2013; Rutqvist, 2012; Streit and Hillis, 2004; Vidal-Gilbert et al., 2010; Zhang et al., 2013; Zoback and Gorelick, 2012). Coupled reservoir-geomechanical numerical modeling has been shown to be an effective tool to test fault instability and potential shear failure (Cappa and Rutqvist, 2011b; Rutqvist et al., 2008). The potential for mechanical failure and the type and orientation of failure is to a large extent controlled by the three-dimensional initial stress regime. An extensional stress regime is shown to be favourable for shear failure along high-angle faults (60°) that may cut through overburden rock above the pressurized storage zone (Rutqvist et al., 2008). Fault shear rupture and dilation may induce or enhance fault permeability that in turn facilitates the rupture propagation across the overlying caprock (Cappa and Rutqvist, 2011b; Rinaldi and Rutqvist, 2013). The effect of initial permeability on co-seismic (sudden) fault slip has been investigated by Cappa and Rutqvist (2011a; 2012) and Mazzoldi et al. (2012), indicating relatively minor impact of initial permeability. Additionally, it was found that that high-permeable fault is likely reactivated later in time than low-permeable fault due to easier fluid pressure dissipation along the fault (Cappa and Rutqvist, 2011a). However, the effect of initial fault permeability on timing, localization and rate of fault shear slip, as well as total aseismic fault slip has not yet been fully investigated.

The high-angle faults located close to CO_2 injection area are usually considered as a probable pathway for CO_2 or brine migration and leakage due to fault permeability, either initial or induced, triggered by shear reactivation (Chang and Bryant, 2008; Barton, 2011; Hannis et al., 2013; Jordan et al., 2013). Here, we investigate if there are any other possible effects of the presence of inclined fault near the injection zone on fluid pressure build-up and buoyancy-driven CO_2 plume migration path using the real geological setting of the St. Lawrence Lowlands region. The deep saline aquifers of the Early Paleozoic sedimentary basin of the St. Lawrence Lowlands (about 200 km x 40 km) are recognized as the best target for the geological storage of CO_2 in the Province of Quebec based on both geologic and practical criteria (Malo and Bédard, 2012). The Cambrian-Lower Ordovician sandstones of the Potsdam Group (Fig. 1) form 200 to 600 m thick reservoir units in the potential storage area (depths < 4 km). The mean total effective capacity for CO_2 storage in the sandstones of the Potsdam Group is 3.18 Gt at the basin scale (Malo and Bédard, 2012). The Utica Shale and siliciclastic rocks of the Lorraine form a comprehensive caprock system (Fig. 1), whose thickness is ranging from 0.8 km to 3.5 km.

The high-angle SW-NE normal faults dipping to the SE affect both the sedimentary succession and the Grenvillian metamorphic basement (Fig. 1). The faults are oriented sub-parallel to oblique (10° to 36°) to the S_{Hmax} stress orientations and are likely near critically stressed for shear slip with slip tendency (shear over normal stress ratio) ranging from 0.34 to 0.58 (Konstantinovskaya et al., 2012). Thus, the initial shear over normal stress ratio is less than the range of 0.6 to 1.0 that would substantially increase the likelihood for shear reactivation. The optimally oriented high-angle normal faults in the area might become unstable under the present-day stress field if fluid pressure during CO_2 injection exceeded the critical threshold 18-

20 MPa for a depth of 1 km, thus increasing the risks of induced seismicity and CO_2 leakages (Konstantinovskaya et al., 2012).

In the present study, coupled reservoir-geomechanical numerical modeling is applied to estimate stress changes related to migration of injected CO_2 and associated increase of fluid pressure P_f in order to evaluate the risk of reactivation of high-angle normal faults in the St. Lawrence sedimentary basin. The coupled reservoir-geomechanical simulator TOUGH-FLAC applied in this case is described in detail by Rutqvist (2011).

The coupled TOUGH-FLAC modeling is performed for the site of the Becancour area (Fig. 2) using a simplified 2D geological model (Fig. 3). The Becancour area is located at about 110 km to the SW from the Quebec City and it is occupied by the industrial park with relatively high CO_2 emissions (between 0.5 and 1 Mt/yr. in 2009) (Malo and Bédard, 2012). The site is easily accessible and has well-developed infrastructures representing one of the best potential sites for CO_2 storage in the St. Lawrence Lowlands (Malo and Bédard, 2012). High density of hydrocarbon exploration wells and seismic lines in the Becancour area made it possible to characterize deep saline aquifers (Tran Ngoc et al., 2012) and to create 3D geological model of the site (Claprood et al., 2012).

The model parameters (main boundary conditions, CO_2 injection rate, initial fault permeability, and permeability of reservoir units) are varied to study their influence on fluid pressure build-up, shear failure of faults and tensile fracturing and to estimate the risk of CO_2 leakage. Permeability of the SW-NE high-angle normal faults that affect the St. Lawrence Lowlands sedimentary succession (Fig. 1) is not well constrained. To evaluate the possible range of fault permeability that may be applied in the numerical simulations, the field observations on fault zone rocks, sample descriptions from fault-crossing wells are analyzed in this study. The fault seal capacity estimation is carried out for the first time in the region for the Champlain and the Yamaska Faults (Fig. 3).

2. MODEL SETUP AND BOUNDARY CONDITIONS

The simplified 2D geological model of the Becancour area (Fig. 3) is oriented NW-SE, across the regional structure (Fig. 2), and it extends vertically from the ground surface to a depth of 4000 m and horizontally 20,000 m. The model is built using interpretation of 2D seismic lines (100 km) and well logs (16 wells), analysis of the seismic map of the top of the Grenvillian basement (Fig. 2) and using a 3D geological model of the Becancour area (Claprood et al., 2012). The 2D simplified model geometry is deemed adequate in this case because the geology in the third dimension (along Y-axis) does not change significantly for several km and because the horizontal principal stresses are orthogonal and parallel to the model section (Fig. 2, Line A-B). This implies that the 2D simplification is adequate from mechanical perspective, in particular to investigate the potential for shear fault reactivation. Moreover, the potential for fault reactivation is driven by changes in reservoir pressure, which is simulated explicitly in the 2D model, but with comparison to pressure evolution calculated with an independent axisymmetric model for the same site (Tran Ngoc et al., 2012). As will be discussed later, it is likely that the current 2D model simplification will result in a lower-bound estimate of the maximum sustainable injection pressure and an upper bound estimate of the potential magnitude of shear slip and rupture length. This is because in a full 3D system, some segments of the fault away from the 2D section would not be pressurized, i.e. where the fault would not be reactivated, and this would tend to restrict shear movements along the faults. On the other hand, there are uncertainties related to the exact orientation of the stress field meaning that the principal stresses might not be exactly parallel and perpendicular to the fault strike, which is not always a planar surface, thus leading to strike-slip fault reactivation, an analysis that would require a 3D model analysis.

The model represents a multilayered CO_2 storage system (Fig. 3) built as a 2D plane-strain model with an arbitrary thickness of 100 m along the Y-axis. It includes (from base to top): low-permeable Grenvillian metamorphic basement, sandstone units of aquifer 1 (Covey Hill Formation) and aquifer 2 (Cairnside Formation), intermediate units (sandstones of the Theresa Formation, dolomites of the Beauharnois Formation and argillaceous limestones of the Chazy, Black River and Trenton Groups) and low-permeable units of caprock 1 (Utica shales) and caprock 2 (fine-grained siliciclastic rocks of the Lorraine Group). The intermediate units are characterized by variable and generally low matrix permeability that is locally enhanced by fracturing or secondary porosity. The sandy limestones of the Lower Chazy Group contain thin (first meters) relatively high-permeable levels but they are not distinguished at the scale of the model.

The sandstones of aquifer 1 of the Covey Hill Formation (Fig. 3) are targeted for CO_2 injection because these rocks are characterized (Table 1) by the highest cumulative thickness

(188 m) of permeable (netpay) levels and matrix permeability (2.6e-16 m^2 or 0.26 mD) if compared to other units, as well as by good porosity (6%). The sandstones of the Covey Hill Formation are located at depths where injected CO_2 would be in supercritical state under the observed fluid pressure and temperature (Table 2) (Tran Ngoc et al., 2012).

The average porosity and matrix permeability of rocks in the reservoir and the caprock sedimentary units (Table 1) of the St. Lawrence Lowlands sedimentary succession were determined from available core analyses (Tran Ngoc et al., 2012). The rock mass permeability that takes into account the presence of natural fractures is not well constrained in the Becancour area because drill stem test (DST) data are rather scarce and non-uniform across the sedimentary succession. To overcome the uncertainty, the rock mass permeability of the reservoir units (Covey Hill and Cairnside Formations) is varied as 10-x (k_1) and 100-x (k_2) values of matrix permeability k_m (Table 1), remaining within the known range of DST data from $4*10^{-15}$ m^2 to 10^{-13} m^2 (4 to 100 mD) in the Becancour area (Tran Ngoc et al., 2012). For the overlying units, the matrix permeability is applied. The permeability of the caprock units of the Utica Shale and the Lorraine Group is taken $10^{-18}m^2$ (Table 1) as determined from the laboratory analyses.

Capillary pressure, CO_2-brine relative permeability, partial miscibility of CO_2 and brine and reactivity of CO_2 with rock matrix affect fluid pressure build-up under constant injection rates (Burton et al., 2009, Bennion and Bachu, 2008; Mathias et al., 2011a; 2011b; 2013). Capillary properties of sandstones of the Potsdam Group are based on laboratory measurements carried out for core samples using both mercury injection and capillary centrifuge tests (Tran Ngoc et al., 2012). The van Genuchten (1980) model for capillary pressure and the van Genuchten-Mualem / Corey model for relative permeability of gas and liquid phases (Corey, 1954) are fitted to laboratory measurements. Capillary properties for the CO_2-brine fluid system are obtained based on conversions from air-mercury and air-brine systems, using the experimental correlation of interfacial tension between CO_2 and brine proposed by Bachu and Bennion (2009).

Entry pressure (Table 1) is estimated 44.1 kPa in sandstones of the Covey Hill Formation and 40 kPa - of Cairnside Formation (Tran Ngoc et al., 2012), with similar value being applied to other units. Entry pressure for CO_2 in shales is generally higher, ranging from less than 0.1 to 10 MPa (Al-Bazali et al., 2005; Busch and Amann-Hildebrand, 2013; Carles et al., 2010; Chadwick et al., 2008; Hildenbrand et al., 2004; Song and Zhang, 2013) and it could be expected value applicable for the modeled fault zones, which are assumed to have the hydrological properties of the Utica shales in the Becancour area (see section 3.1 below). However, the above quoted values are laboratory scale properties, whereas in the field caprock units and faults include discontinuities, such as fractures and minor secondary faults that may be slightly more permeable, resulting in a lower capillary entry pressure. In these simulations we assumed the same entry pressure of 40 kPa, which is not unrealistic considering a shale permeability of 1×10^{-18} m^2 (Busch and Amann-Hildenbrand, 2013), but it might be considered as a lower limit value for the shaly caprock units and the fault zones to simulate the worst scenario when the presence of natural fractures might facilitate fluid circulation. In any case, a CO_2 injection over-pressure of a few MPa will be sufficient to break the capillary barrier and the caprock units and faults will be considered permeability seals, rather than capillary seals (Rutqvist, 2012).

The poroelastic constitutive model of the rock mass is applied in simulations, whereas faults follow an elasto-plastic behavior represented by the anisotropic ubiquitous-joint model implemented in FLAC3D (Itasca, 2009). The elastic properties (Table 1) of sedimentary rocks have been determined from triaxial strength tests carried out on core samples in the Weatherford Laboratory. The values of measured (E, ν) and calculated (K, G, λ) elastic moduli (Table 1) indicate dolomitic sandstones of intermediate units (Theresa Formation) are more rigid and more brittle than other aquifer and intermediate units, and calcareous shales of caprock 1 (Utica Shale) are more brittle than siliciclastic rocks of caprock 2 (Lorraine Group). The rocks of the Theresa Formation and the Utica Shale are thus expected to be the first units that would be affected by tensile fracturing in the sedimentary succession of the St. Lawrence Lowlands.

The Biot's coefficient α in simulations is assumed equal 1 for all units (Table 1). Its value may be estimated from the equation (Zoback, 2010):

$$\alpha = 1-K_{dry}/K_0,$$

where K_{dry} is the bulk modulus of dry (drained) rock and K_0 is the bulk modulus of the rock's individual solid grains. The bulk modulus K_{dry} for the studied sedimentary units is calculated from values of Young modulus and Poisson's ratio (Zoback, 2010) that were measured during laboratory tests on drained core samples (K in Table 1). The average bulk modulus of mineral grains might be approximate as 37 GPa for quartz, 37.5 GPa for average feldspar, 95 GPa for dolomite, and 77 GPa for calcite (http://subsurfwiki.org/wiki/Elastic_properties_of_common_sedimentary_rock_forming_minerals). Applying these values in the above equation, the Biot's coefficient is about 0.56 for sandstones and 0.67 for dolomites, except the Cairnside Formation where it is ~0.2. From laboratory experiments reported in the literature, it is clear the Biot's coefficient could be considerably lower than 1, and it is also stress-dependent along with the stress decency of the bulk modulus (Coussy, 2004). In our simulations, the Biot's coefficient will have an impact on the reservoir strain induced by the fluid pressure (mostly in the vertical direction) and on the poro-elastic stress (mostly induced in the horizontal direction). Regardless of the choice of Biot's coefficient, the Terzaghi effective stress measures the stress level sustained by the solid matrix and it is conventionally used to detect failure in a plastic material (Coussy, 2004; Itasca 2009). Thus, the potential for failure depends mostly on the fluid pressure within the fault in relation to the external stress field with some impact of poro-elastic stress (Rutqvist et al., 2008). Our use of a relatively high Biot's coefficient will result in a relatively larger vertical expansion of the reservoir and a higher induced shear stress on the bounding faults, which in turn might result in an earlier fault reactivation (at a lower injection pressure) and a larger shear displacement once the fault is reactivated.

The multilayered storage system is generally flat-lying (Fig. 3) and it is affected by two high-angle (60°) normal faults (Champlain Fault and Yamaska Fault) that extend SW-NE (Fig. 2) and dip to the SE, displacing the sedimentary units downward to the SE. The Yamaska Fault is located at a shorter distance (1.5 km) from the injection zone, while the Champlain Fault is more distant (4.4 km). The normal faults are designed in the model as 30 m wide. According to applied ubiquitous-joint model, a series of parallel weak planes (joints) with a dip angle of 60◦ and a spacing of 10 m is assigned within the fault. Weak planes are assumed to have a normal and shear stiffness of 5 GPa/m, and designed with cohesion 0.5 MPa, with a friction angle of 25°, a dilation angle of 0° and no tensile strength. For simplicity, the faults are extended up to the surface in the model (Fig. 3), although no upward continuation of fault planes was interpreted on seismic lines (Fig. 1, cross-sections) above the top of the Utica Shale, probably due to syn-sedimentary nature of faults.

The block modeled for CO_2 injection in the Becancour area is located between the Champlain and the Yamaska Faults (Fig. 3). The vertical well A198 SOQUIP Petrofina Becancour No 2 is used for simulation of CO_2 injection because it is one of few wells that penetrate the bottom of reservoir unit of the Covey Hill Formation and it is not located too close to the Yamaska Fault (Figs 2, 3). The injection zone or bottom of the injection well is located at X =

10275 m, Z = - 1180 m, at 1540 m from the Yamaska Fault and at 4430 m from the Champlain Fault (Fig. 3).

The NW-SE West and East Transverse Faults bound the modeled block in the SW and the NE, respectively (Fig. 2). The East Transverse Fault is suggested from the analysis of the time structure of the Grenvillian basement (Thériault et al., 2005). The West Transverse Fault is interpreted as a lineament detected from the remote sensing data (Matton et al., 2011), which is correlative with a strong linear gradient of the magnetic survey data, and across which high variation of fluid pressure gradient (Fig. 2) is observed.

The average maximum in-situ horizontal stress (S_{Hmax}) in the St. Lawrence Lowlands (Fig. 1) is oriented N59°E±20° (Konstantinovskaya et al., 2012). The stress gradients (Table 2) in the region have been previously estimated for depths < 4 km (Konstantinovskaya et al., 2012) as ΔS_{hmin} 20.5±3 kPa/m, ΔS_v 25.6 kPa/m, ΔS_{Hmax} 40±7.5 kPa/m, that indicates a strike-slip stress regime with $S_{hmin}<S_v<S_{Hmax}$ (Konstantinovskaya et al., 2012). The 2D model of the Becancour area is oriented sub-parallel to S_{hmin} (X-axis) and S_v (Z-axis) and sub-orthogonal to S_{Hmax} (Y-axis) stresses (Fig. 2). As the model is two-dimensional and orthogonal to S_{Hmax} orientation (Fig. 3), the relation between two principal stresses acting in the model plane ($S_{zz}=S_v$ and $S_{xx}=S_{hmin}$) corresponds to the extensional stress regime ($\Delta S_{hmin}=0.7\Delta S_v$), where ΔS_{hmin} is equal to 18 kPa/m (Table 2).

The average fluid pressure P_{f0} gradient is estimated from the analysis of drill stem test (DST) data in vertical wells (Konstantinovskaya et al., 2012) and it is about 9.8 kPa/m for the St. Lawrence Lowlands. The fluid pressure gradient is elevated to an average of 12.17 kPa/m (Table 2) within the modeled block of the Becancour area (Fig. 2) that is compatible with the elevated brine density 1.13–1.29 g/cm^3 and salinity (Table 1) in this area (Massé, 2009). The higher value of P_{f0} gradient of 15.6 kPa/m is observed to the SW of the West Transverse Fault in the Becancour area (Fig. 2) that likely indicates the presence of a separate confined reservoir and may be associated with the sealing character of the fault. The fluid pressure gradient to the NW of the Champlain Fault is 10.4 kPa/m (L. Massé, personal communication).

The temperature gradient (Table 2) in the Becancour area is 23.5°C/km with an average surface temperature 8°C (Tran Ngoc et al., 2012).

With the above gradients, the minimum principal stress at the depth of the injection zone around the injection well (about 1 km depth) is about 18 MPa, whereas the vertical stress is about 26 MPa. Moreover, the initial reservoir pressure is about 12 MPa and initial temperature is about 31 °C. Thus, a pressure build-up of 6 MPa would lead to well pressure of a magnitude similar to that of the minimum principal stress. This might be relevant when considering limits on the injection pressure as an injection pressure about the minimum principal stress could theoretically lead to the formation of a vertical hydraulic fracture. However, the injection-induced stress evolution is more complex and we also need to consider the potential for fault reactivation as will be considered in the current reservoir-geomechanical model simulations.

Constant pressure, saturation, and temperature conditions are assumed at the top and bottom boundaries of the 2D model (Fig. 3). The left and right boundaries are closed for fluid and heat flow. Null displacement conditions are set normal to the left, right and bottom boundaries, whereas stress is set to the top, left and right boundaries. Note though that the left and the right boundaries are far away from the hydraulically bounding faults meaning that whether they are simulated as open or closed boundaries, it does not have an impact on the simulation results at the central part of the model. All simulations presented in this study are carried out as isothermal, i.e. without taking into account the cooling effect of injected CO_2. The maximum time of injection is 30 years.

3. RESULTS

The observation of fault zone rocks and estimation of fault seal capacity are first discussed in order to evaluate the likely range of fault permeability that may be attributed to the Champlain and the Yamaska Faults in the reservoir-geomechanical modeling of CO_2 injection in the Becancour area.

3.1 Fault permeability

The vertical offset of high-angle normal faults in the St. Lawrence Lowlands is varying along their strike (Fig. 1) that results in lateral change of lithological units superimposed across the fault plane. For example, the vertical offset across the Saint-Cuthbert Fault progressively grows toward the NE varying from 30 m at its SW tip, where limestones of the Trenton Group are superimposed (Fig. 1), up to 367 m in its central segment, where the fault separates the Grenvillian basement and limestones of the Trenton Group (Globensky, 1987 and references therein). The along-strike variation of vertical offset of faults controls the composition of fault zone rocks and the volume of shales slipped along fault planes and, consequently, the sealing capacity of faults.

The possible range of permeability of the Yamaska and the Champlain Faults buried below caprock units in the Becancour area (Fig. 1) is evaluated from (1) observations of comparative faults zones exposed at the surface on the northern shore of the St. Lawrence River, (2) the description of cuttings from well A027 Saint-Angele No 1 that penetrates the Yamaska Fault zone (Fig. 2), and (3) 2D estimation of fault seal capacity based on shale-gouge ratio and well-log data.

3.1.1 Fault zone rocks

The field observations of fault zones (Fig. 1) were collected along the major normal faults exposed at the surface on the northern shore of the St. Lawrence River including the Saint-Cuthbert, Saint-Alban, Deschambault, Jacques Cartier, Neuville, Montmorency and Cap Tourmente normal faults that belong to the same system of the SW-NE high-angle normal faults as the Champlain and the Yamaska Faults.

The studied fault zones are generally composed of fragmented wall rocks, whose composition depends on the vertical offset of faults (Fig. 1). The SW segment of the Saint-Cuthbert Fault and the Saint-Alban Fault are characterized by low (<30 m) vertical offset displacing argillaceous limestones of the Trenton Group. The fault rocks along these faults are represented by shale-cemented calcareous breccia. The normal faults with greater vertical throw separate the caprock units (Utica Shale and Lorraine Group) and the Grenvillian basement (Fig. 1). The Neuville (202 m) and the Montmorency (>180 m) faults, which are exposed at the surface, and the Champlain (>300 m) and the Yamaska (>800 m) faults that are buried at depth, belong to this group of faults.

The Montmorency Fault in the Quebec City area (Fig. 4a) represents the eroded analog of the Yamaska and the Champlain Faults in the Becancour area (Fig. 3). The footwall of the Montmorency Fault is composed of metamorphic rocks of the Grenvillian basement recovered by relatively thin relic layers of limestones of the Trenton Group. The hanging wall consists of limestones of the Trenton Group, Utica shales and siliciclastic rocks of the Lorraine Group. The vertical offset of the Montmorency Fault is estimated to be at least 180 m if the minimum thickness of the Trenton Group is taken as 100 m (Fig. 4a). However, the vertical offset is likely to be greater (300-400 m) as thickness of the Trenton Group in closely located wells is varying from 190 m to 335 m (drilling reports for wells A257and A175, see Appendix).

The fault zone of the Montmorency Fault (Fig. 4b) is filled with continuous 15-20 cm-thick smears of calcareous shales dragged into the fault plane from the shale interlayers of the Trenton Group in the hanging wall. The shales smears in the fault zone and in the upper part of the Trenton Group are similar in composition to the overlying Utica calcareous shales. The boudinated lenses of limestones are dragged in the fault zone and extended parallel to the fault plane within the calcareous shale matrix (Fig. 4b). The gneisses of the footwall demonstrate ductile deformations, sinistral strike-slip horizontal striation and contain zones of cataclastic breccia 30-40 cm thick. The breccia is composed of angular gneissic fragments, which are solidly cemented by fine-grained crushed gneiss matrix.

The presence of shales smeared along the fault plane as a 15-20 cm-thick continuous layer is strongly supportive for the sealing behaviour of the observed segment of the Montmorency Fault. This continuous shale smears have been formed in the fault segment, along which only the Trenton Group is downthrown for at least 180 m, while the overlying Utica shales of the hanging wall are located above the observed fault segment (Fig. 4a). One may expect that the presence of continuous shale smears is even more probable for the faults with higher vertical offset, such as the Champlain (300-550 m) and the Yamaska (800-1200 m) Faults (Table 3), because not only the Utica shales but also the major part of the Lorraine Group are slipped along their fault planes (Fig. 3).

The Yamaska Fault was penetrated by well A027 Sainte Angele No 1 (Fig. 2), which cut through the caprock units of the Lorraine Group and the Utica Shale and the intermediate units of the Trenton Group and entered granite and metamorphic rocks of the Grenvillian basement at depth of 1553 m. According to the description of cuttings from the well (Farish, 1933), the contact between the limestones and the metamorphic rocks is faulted. The transition zone (about 3 m) is composed of dark grey calcareous shales with well-marked slickensides and calcite vein. The observations of highly saline water were reported during the drilling along the faulted contact between the Trenton Group and the Precambrian.

3.1.2 Fault seal capacity

Fault seal capacity for the Champlain and the Yamaska Faults is estimated along 2D vertical cross-sections (Fig. 5) using the shale gouge ratio (SGR) method (Freeman et al., 1998; Yielding et al., 1997). The SGR at a given point on a fault plane is estimated as a volume of shale in slipped interval past the point:

$$SGR = \Sigma (V_{sh} \times \Delta z) / t \times 100\%,$$

where V_{sh} is the volume of shale in a given unit, Δz is the thickness of the unit, and t is the throw window. The volume of shale is calculated using natural radioactivity (GR) of rocks from well log data (Doveton, 1986):

$$V_{sh} = (GR-GR_{clean})/(GR_{shale}-GR_{clean}),$$

where GR is radioactivity of a given rock interval, GR_{clean} is the baseline of lowest radioactivity rocks and GR_{shale} corresponds to the baseline radioactivity of 'normal' shales (as opposed to uranium-rich shales). The shale volume in the lithological units decreases from 0.95 at the top to 0.1 at the base of the St. Lawrence Lowlands succession (Table 3).

The vertical offset (throw) is increasing downward along the Champlain and the Yamaska Faults (Table 3) because continued slip has occurred along the fault planes during the sedimentation as a result of the Taconic orogeny and progressive deepening of the St. Lawrence Lowlands basin.

The shale gouge ratio progressively increases upward from 7% to 95% along the Champlain and the Yamaska Faults (Fig. 5) as the volume of shale in the slipped hanging wall grows toward the top of the stratigraphic succession (Table 3). The SGR > 15-20% usually characterizes faults with presence of shale smears on the fault plane and static sealing behaviour (Yielding et al., 1997). For example, the fault from the Oseberg Syd Field of the Norwegian shelf with SGR 18% seals and it is able to support a minimum cross-fault pressure difference of 0.8 MPa (Freeman et al., 1998). Accordingly, the upper fault segments of the Champlain and the Yamaska Faults with SGR > 17-21% (Fig. 5) would likely have continuous shale smears and behave as a seal. Indeed, the shale smears similar in composition to the Utica calcareous shales were observed in the Yamaska fault zone in well A027 (Farish, 1933).

The Yamaska Fault is thus expected to have sealing behaviour along the segment with SGR >17%, which is located at the same level and above the footwall reservoir sandstones of the Covey Hill Formation targeted for CO_2 injection (Fig. 5b). The upper segment of the Champlain Fault with SGR>21% must also be sealing (Fig. 5a). The lower segment of the Champlain Fault with SGR 7-11% might be permeable but fault-orthogonal fluid flow across the lower fault segment is very unlikely due to the presence of low-permeable rocks of the Grenvillian basement on the opposite side of the fault plane (Fig. 5a). The sealing behaviour of the Champlain Fault in the Becancour area is supported by variations in fluid pressure observed on each side of the fault (Fig. 2).

3.2 Reservoir geomechanical coupled simulations

Three injection rates of 0.06 kg/s, 0.3 kg/s and 1kg/s are tested by numerical simulations (Table 4) to predict fault stability during CO_2 injection in the Becancour 2D model. The absolute values of the used injection rates are set lower than the full 3D field values because of the very restricted width (100 m) of the 2D model along the Y axis (Fig. 3) that otherwise results in unrealistically rapid fluid pressure build-up around the injection well. The pressure build-up achieved for an injection rate of 0.06 kg/s in the 2D model with Y axis of 100 m is consistent with the pressure build-up at 3D injection rate of 4.5 kg/s (0.15 Mt/yr.) simulated in radial model with radius of 3.5 km by Tran Ngoc et al.(2012). The injection rate of 0.1-0.2 Mt/yr. is applied in pilot and small-scale CCS projects (GCCSI, 2012). The injection rates of 0.3 kg/s and 1 kg/s in the 2D model may be correspondingly compared with the 3D injection rates of 23 kg/s (0.8 Mt/yr.) and 75 kg/s (2.5 Mt/yr.), respectively (Table 4). These injection rates are compatible with CO_2 volumes stored in large-scale integrated CCS projects (GCCSI, 2012). It is the rate of pressure build-up and the pressure magnitude relative to the in situ stress field that is most important for the potential and timing of fault reactivation (Rutqvist, 2012). By varying the injection rate we consider a range of pressure build-up and pressure magnitudes that might occur at the real field setting when exposed to the injection.

Two values of fault permeability are tested: 10^{-18} m^2 for the sealing fault behaviour and 10^{-16} m^2 for the permeable fault (Table 4). In first case, fault permeability is equal to the permeability of the Utica shales (Table 1) that is supported by A027 well data and field observations (Fig. 4b) and by the composition of the hanging wall slipped past the reservoir units of the Covey Hill Formation in the footwall (Fig. 5b). In second case, fault permeability is equal to the matrix permeability k_m of the reservoir sandstones (Table 1). The permeable fault behaviour is tested because in some cases, strong directional permeability contrast may exist along the fault damage zone allowing along-fault fluid circulation even if orthogonal fluid flow is closed (Agosta et al., 2012; Arch and Maltman, 1990). The higher fault permeability may also be induced as a result of brittle and dilatant deformations related to shear slip and volumetric changes of fault material under critical state when the fluid pressure approaches the minimum horizontal stress.

Two values of rock mass permeability are tested for the reservoir units of the Covey Hill and the Cairnside Formations (Table 4) assigned as 10-x (series 1, k_1) and 100-x (series 2, k_2) higher than respective values of matrix permeability k_m of these units (Table 1).

The resulting variations in several parameters (Tables 5 and 6) are analysed during the simulations as a function of changes in initial values of injection rate, fault and reservoir permeability (Table 4). We analysed the fluid pressure build-up around the injection well (Figs 6, 7a), vertical surface uplift above the injection zone (Fig. 7b), effective shear strain increment (a measure of the shear strain from the start of the injection defined as the second invariant of the deviatoric strain tensor) in the injection zone and along fault zone (Figs 7d, 8-11; 14), slip along the Yamaska Fault (Fig. 7c), tensile fracturing above the injection zone (Fig. 12) and CO_2 plume growth and displacement (Fig. 13). The potential for tensile fracturing is calculated using the assumption that a tensile failure may occur in a unit as fluid pressure exceeds the minimum compressive stress, i.e., in the Becancour 2D model, the effective stress S_{hmin}*=S_{xx}* becomes positive.

Series 1. Low reservoir permeability k_1=10k_m

Simulation 1a (injection rate 0.06 kg/s, sealing fault behaviour).

The fluid pressure increases around the injection well within the sedimentary succession below the caprock 1 of the Utica Shale (Fig. 6a). Most of the fluid pressure build-up occurs between the injection well and the Yamaska Fault, while the pressure increase is much less significant in the direction of the Champlain Fault (Fig. 6a). At the beginning, the fluid pressure build-up in the injection zone is higher than at the Yamaska Fault but it equalises in these areas at the end of run (Fig. 7a). The fluid pressure increase is 1.8 MPa around the well, 1.7 MPa at the

Yamaska fault and 0.5 MPa at the Champlain Fault after 30 years of injection (Fig. 7a, Table 5). The vertical surface uplift above the injection well is 2 cm at the end of run 1a (Fig. 7b).

Injection-induced shear strain occurs mostly around the injection zone within the Covey Hill reservoir unit propagating laterally with time (Fig. 8). The magnitude of shear strain in the Yamaska fault zone remains smaller than around the well (Fig. 7d; Table 5) and no fault reactivation is observed (Fig. 8). No significant shear strain occurs along the Champlain fault.

The effective horizontal stress S_{xx}* remains negative (i.e. compressive) within and above the injection zone (Fig. 12a). The CO_2 plume is about 0.5 km wide after 30 years of injection (Fig. 13a; Table 5).

Simulation 2a (injection rate 0.3 kg/s, sealing fault behaviour).

The fluid pressure increases up to 8.3 MPa and 7.5 MPa around the well and in the Yamaska Fault, respectively, at a simulation time approaching 30 years (Fig. 7a, Table 5). The vertical displacement (uplift) of the surface above the injection well is 9 cm at the end of the run (Fig. 7b).

The injection-induced shear strain (Fig. 7d) in the injection zone is the same as in the Yamaska Fault until the fault is reactivated as a normal fault at 22.5 years. At this time, the injection-induced pressure increase is about 7 MPa at the well and 6.5 MPa at the Yamaska fault. That is, the well pressure has increased from an initial 12 MPa (at about 1 km depth) to 19 MPa, which is just above the minimum principal stress magnitude. After reactivation, the shear strain increases more rapidly along the fault than around the well (Fig. 7d). The Yamaska fault is initially reactivated below the caprock units, within the 300 m-long fault segment that separates the intermediate units (Beekmantown and Trenton Groups) in the footwall from the caprock 2 (Lorraine Group) in the hanging wall (Fig. 9b). During subsequent steps (Fig. 9b-d), the slip along the fault propagates both upward and downward but remains below the caprock 2 units. The Champlain Fault is not affected by deformation in this simulation.

The slip along the Yamaska Fault zone is 1 cm (Fig. 7c) and the length of the reactivated segment is 600 m at 30 years (Fig. 9d). Note that in these simulations the fault reactivates gradually and in a stable aseismic manner over many years of pressure build-up. This is related to the perfectly plastic constitutive model applied to the fault in this case, whereas more abrupt slip events could occur if using a strain-softening plastic model as in Cappa and Rutqvist (2011a).

Nevertheless, the timing for the initiation of fault reactivation and the total slip at the end of the simulation will be similar for perfectly plastic and strain-softening models.

The effective minimum horizontal stress S_{xx}* is reduced to -2 MPa in the area above the injection zone due to the increase of fluid pressure but it remains negative (i.e. in compression) (Fig. 12b; Table 5). Thus, even though the injection pressure has exceeded the initial minimum principal stress in the injection reservoir, the effective minimum stress is still in compression and hydraulic fracturing would not occur. The effective minimum stress still remains in compression because the pressurization of the reservoir also results in an increase in horizontal stress within the reservoir. Such local reservoir stress change along with injection or production is a well-known phenomenon in oil and gas reservoir engineering and results from poro-elastic stress changes that have an impact on the potential for tensile and shear failure within and around the reservoir (Hawkes et al., 2005; Rutqvist, 2012; Rutqvist et al., 2008). The CO_2 plume is about 0.9 km wide after 30 years of injection (Fig. 13b; Table 5).

Simulation 3a (injection rate 0.3 kg/s, permeable fault behaviour).

The fluid pressure build-up around the injection zone and in the Yamaska Fault in run 3a is the similar to that of run 2a reflecting the same injection rate (Fig. 7a, Table 5). The total increase in vertical surface uplift above the injection zone is 9 cm at the end of run 3a, which is also similar to run 2a (Fig. 7b; Table 5).

Shear strain localizes along the Yamaska fault earlier than in run 2a, at 18.2 years of injection (Fig. 7c). Thus, fault reactivation is initiated at a slightly lower injection pressure probably as a result of more rapid pressure diffusion into the fault. Shear slip initially localizes in the 60 m-long fault segment that separates the caprock 1 (Utica Shale) in the footwall and caprock 2 (Lorraine Group) in the hanging wall (Fig. 10b). After the reactivation, shear failure along the Yamaska fault progresses upward and downward (Fig. 10c), eventually reaching the surface (Fig. 10d). The slip along the Yamaska Fault is 4 cm at 30 years (Fig. 7c; Table 5). No shear strain increase occurs along the Champlain Fault.

The increase in effective minimum horizontal stress S_{xx}* in simulation 3a is the same as in run 2a and it remains negative (i.e. compressive) (Table 5). The CO_2 plume is about 0.9 km wide after 30 years of injection (Fig. 13b).

Simulation 4a (injection rate 1.0 kg/s, sealing fault behaviour).

The fluid pressure build-up in run 4a is higher than in the previous simulations and it reaches 18.8 MPa at the well and 16 MPa at the Yamaska Fault after 17.9 years of injection (Fig. 7a, Table 5). The vertical surface uplift above the injection well reaches 20 cm at 17.9 years (Figs 7b).

The increase in shear strain is concentrated along the Yamaska Fault at 7.3 years (Fig. 11b), signifying the initiation of fault reactivation. At this time, the pressure build-up has reached 12 MPa at the injection well and about 7 MPa at the Yamaska fault (Table 5). Thus, the pressure build-up at the Yamaska fault leading to fault reactivation is about the same as run 2a and 3a. The 7 MPa pressure build-up at the Yamaska fault represents a total pressure of about 19 MPa, which is just above the minimum principal stress (about 18 MPa), whereas the total pressure at the injection well (about 24 MPa) is much higher than the minimum principal stress. The shear slip is initiated along the 330 m-long fault segment that separates the intermediate units (Cairnside and Theresa Formations) in the footwall and the caprock 2 units (Lorraine Group) in the hanging wall (Fig. 11b). The fault reactivation progressively propagates upward and downward affecting the whole sedimentary succession at 17.9 years (Fig. 11c-d). The increase in - shear strain grows faster along the fault than in the injection zone after the fault is reactivated at 7.3 years (Fig. 7d). The slip along the Yamaska Fault is 12 cm and 17 cm after 17.9 and 30 years of injection, respectively (Fig. 7c; Table 5).

A zone of positive effective minimum horizontal stress S_{xx}* starts to form above the injection zone within the intermediate units of the Trenton Group and the Theresa Formation after 10 years of injection (Fig. 12c; Table 5). At 17.9 years (Fig. 12c), the zone of positive S_{xx}* involves the area between the top of aquifer 2 (Cairnside Formation) and the base of caprock 1 (Utica Shale) due to strong fluid pressure build-up (Fig. 7a) localized below the caprock units. The positive values of the effective horizontal stress testify for the potential of tensile fracturing in the more fragile (Table 1, Young modulus) intermediate units. However, the thick part (460 m) of the caprock 2 units (Lorraine Group) likely remains intact where S_{xx}* is still negative, i.e. in compression (Fig. 12c).

The CO_2 plume grows about 1.7 km wide after 30 years of injection (Fig. 13c). The plume spreads asymmetrically, faster in the NW direction, away from the Yamaska Fault, and slower toward the fault (Fig. 13c). The upward migration of the CO_2 plume is limited by the base of the intermediate units (Theresa Formation).

Series 2. High reservoir permeability $k_2=100k_m$

Fluid pressure increases more homogeneously over the large area between the Champlain and the Yamaska Faults in simulations 1b-4b (Fig. 6b) if compared to runs 1a-4a (Fig. 6a). High rock mass permeability of the reservoir units (Table 4) results in rapid fluid propagation away from the injection well and fast fluid flow dispersion in the aquifers between two reservoir-bounding faults. Consequently, fluid pressure build-up in high-reservoir permeability runs 1b-4b is systematically lower than in the previous simulations 1a-4a for corresponding injection rates (Fig. 7a). The increase of fluid pressure in the injection zone and at the Yamaska Fault equalises very rapidly, after 5-10 years of injection (Fig. 7a; Table 6). The surface vertical uplift above the injection well is less significant if compared to the runs of series 1 (Fig. 7b; Table 6).

The Yamaska Fault is not reactivated after 30 years of injection in simulations 1b-2b with sealing fault behaviour. Shear slip occurs along the 60 m-long fault segment after 27.5 years of injection (Fig. 7d; Table 6) and reaches 0.5 cm at 30 years (Fig. 7c) in run 3b with injection rate 0.3 kg/s and permeable fault properties (Table 6). Shear failure occurs along the 330 m-long segment of the Yamaska Fault at 7.8 years in run 4b at an injection rate of 1 kg/s (Figs 7d, 14a) and shear slip is 10 cm at the end of run (Fig. 7c; Table 6). In both cases in which reactivation occurred (3b and 4b), the reactivation occurred once the total fluid pressure at the Yamaska fault reached a magnitude similar to that of the minimum principal stress.

The Champlain Fault remains stable in series 2 runs and it is reactivated only in run 4b with high injection rate after 30 years of injection (Fig. 14d; Table 6). The fluid pressure build-up in the hanging wall of the fault increases up to 16 MPa after 30 years of injection. The shear failure occurs along the deep-seated 500 m-long fault segment that separates the reservoir units of the Covey Hill Formation in the hanging wall and the Grenvillian basement in the footwall and continues below the reservoir level (Fig. 14d). The relative displacement along the Champlain Fault reaches 2.5 cm.

The effective minimum horizontal stress S_{xx}* remains negative (i.e. in compression) and tensile fracturing does not occur in the simulations with high reservoir permeability except in run 4b with high injection rate (Table 6). In this case, tensile fractures may start to form locally in the intermediate unit of the most fragile (Table 1) Theresa Formation at 17.8 years. The zone of positive S_{xx}* (Fig. 12d) is much less important than in run 4a at 17.9 years (Fig. 12c). As the fluid pressure increases below the caprock units, the zone of positive S_{xx}* grows progressively in run 4b and involves all intermediate units (Beekmantown and Trenton Groups) and the base of caprock 1 (Utica Shale) after 30 years of injection (Table 6). The S_{xx}* remains lower in run 4b (Table 6) than in run 4a (Table 5) at 30 years.

The CO_2 plume grows wider, up to 2 km, (Fig. 13d; Table 6) in the high-reservoir permeability runs than in simulations with low reservoir permeability under the same injection rate (Fig. 13c; Table 5). The vertical migration of the CO_2 plume is also more pronounced in the simulations with high-reservoir permeability and low and medium injection rates (Figs 13a, b). Similar to the runs of series 1, the CO_2 plume propagates asymmetrically, faster in the direction opposite to the Yamaska Fault (Fig. 13b, d) as the fluid pressure build-up between the fault and the injection well is more significant than toward the Champlain Fault (Fig. 6b).

4. DISCUSSION

The coupled reservoir-geomechanical (TOUGH-FLAC) modeling undertaken in this study shows that fluid pressure build-up around the injection well and in the Yamaska fault zone strongly depends on the injection rate: the higher is the injection rate, the stronger is the fluid pressure build-up observed around the well and in the fault zone at the end of run (Fig. 7a, Tables 5 and 6). Moreover, the simulation shows that the initiation of fault reactivation at the Yamaska is strongly dependent on the pressure build-up at the fault. The increase of fluid pressure in the injection zone is higher than along the Yamaska fault at the beginning of injection and it equalizes at about 30 years (Fig. 7a) due to lateral fluid flow from the well to the fault. The fluid pressure equilibrium is achieved faster, after 5-10 years of injection, in the simulations 1b-4b with high reservoir permeability (Fig. 7a).

The model setting parameters applied in 2D plane strain model of the Becancour area more likely characterise a lower bound of the maximum sustainable injection pressure and an upper bound of possible fault slip magnitude and rupture area. As mentioned, this is because in a full 3D system, there are segments of the fault away from the 2D section that would not be pressurized and where the fault is not reactivated that would tend to restrict shear movements along the faults. Moreover, the global permeability of the reservoir units might be higher than applied in simulations 10^{-15}-10^{-14} m^2 (Table 4) due to the presence of extensive natural fractures that means fluid pressure build-up in the injection zone and at the faults would be lower as it is supported by respective changes of ΔP_f observed in series 1 and 2 runs (Fig. 6). Additionally, the width of faults is taken as 30 m and the entry pressure of fault rocks - at low value of 40 kPa to test the worst case of high conductivity along fault plane. However, the field data presented above suggest fault width of the Montmorency and the Yamaska faults is rather limited by 10 m maximum, at least for the upper 1.5 km of depth, and their fault planes contain shale smears, the rocks that generally characterized by much higher entry pressure (e.g. AL-Bazali et al., 2005). If these considerations are taken into account, the risk of fault reactivation as presented in our simulations is overestimated. The better constraints on CO_2-brine relative permeability and rock compressibility of the intermediate and caprock units would be helpful in sensitivity analysis of shear-slip risk evaluation as these parameters may affect the injection-induced fluid pressure build-up (Mathias et al., 2011a).

Fluid pressure increase around the injection zone is asymmetrical, being higher in the area between the injection zone and the Yamaska Fault than toward the more distant Champlain Fault (Fig. 6). The lateral fluid flow toward the Yamaska Fault is restrained within short-distance area (1.5 km) by the sealing behaviour of the fault and/or the low-permeable caprock 2 units (Lorraine Group) in the hanging wall. This results in a higher fluid pressure build-up around the Yamaska Fault than in the opposite direction toward the Champlain Fault (Fig. 6). Consequently, the CO_2 plume grows laterally faster in the direction away from the Yamaska fault (Fig. 13), toward the area with lower fluid pressure build-up.

Fault reactivation is controlled to a large extent by the pressure build-up at the fault which in turn depends on the injection rate and the distance between fault and injection well. The Yamaska Fault located closer (1.5 km) to the injection zone is reactivated more promptly than more distant (4.4 km) Champlain Fault. Higher injection rate results in earlier reactivation of the Yamaska Fault (Fig. 7c) due to higher fluid pressure build-up (Fig. 7a). For example, the Yamaska Fault is reactivated at 7.3 years for an injection rate of 1 kg/s and only at 22.5 years when the injection rate is 0.3 kg/s (Fig. 7c) in simulations of series 1. As a result, the total fault slip is more significant in the simulations with earlier fault reactivation and higher injection rates (Fig. 7c). The Champlain Fault is generally not reactivated; the shear failure along the fault is observed (Fig. 14d) only after 30 years of injection in simulation with high injection rate (1kg/s) and high permeability of reservoir units.

The localization of shear failure along pre-existing high-angle normal faults depends on initial fault permeability. Under the sealing fault behaviour, shear slip on the Yamaska Fault occurs along the fault segment located mostly below the caprock units and above the targeted reservoir in the footwall (Fig. 9b-d). The fluid flow moving from the injection well to the fault zone is likely trapped below the inclined sealing fault plane, where the fluid pressure build-up causes the fault reactivation. When the fault is permeable, shear failure is initiated along the fault segment located within the caprock 1 units of the footwall (Fig. 10b); afterward, it progresses upward and downward reaching the surface (Fig. 10c-d). The fluid flow spreads from the injection well toward the fault and then propagates upward along the permeable fault zone being kept from across-fault lateral propagation by impermeable caprock 2 units (Lorraine Group) of the hanging wall. The fluid pressure is therefore concentrating within the fault zone at the level of the more rigid, brittle and thin caprock 1 unit (Utica Shale) of the footwall, where the first shear slip occurs (Fig. 10b).

The localization of shear failure along high-angle normal faults seems to be also dependent on the location of the injection zone relative to the inclined fault plane. In case of the Yamaska Fault, the injected reservoir is found in the footwall of the fault plane and the shear failure is initiated along the fault segment located above the targeted reservoir (Fig. 9b). In contrast, when the injection is simulated in the hanging-wall reservoir (the Champlain Fault), the rupture occurs along the fault segment located at the reservoir level and below it (Fig. 14d). The result similar to the case of the Champlain Fault was obtained by Cappa and Rutqvist (2001a), who found that the reactivation of a pre-existing high-angle normal fault occurs along the segment located at the reservoir level and below it when CO_2 injection was simulated in the hanging wall of the fault. The difference between the localization of reactivated fault segments in two cases of the reservoir-bounding faults obtained in the present study may be explained by the increase in stresses that occurred in the acute angle between the sealing fault plane and the reservoir due to growing pressure build-up in the reservoir.

The timing of fault reactivation, length of rupture and slip rate are affected by initial fault permeability. In case of the Yamaska Fault, shear slip occurs earlier, at 18.2 years, when the fault is permeable (10^{-16} m^2), and later, at 22.5 years, when the fault seals (10^{-18} m^2) under the same boundary conditions (Fig. 7c, runs 2a and 3a). It might be related to the length of the segment, along which shear failure is initiated. When the fault is permeable, the shear deformation is initiated within shorter (60 m) segment of fault plane (Fig. 10b) if compared to the case of sealing fault (300 m) (Fig. 9b) (Table 5). It might take longer time to produce shear slip along a longer and sealing fault segment than along a shorter and permeable fault segment. The slip progresses faster along the permeable fault than along the fault with sealing behaviour. At 5.5 years after the fault reactivation, shear slip (Fig. 7c; Table 5) reaches 1.5 cm along the permeable fault (3a) and only 0.3 cm along the sealing fault (2a).

The high permeability of the reservoir units (Potsdam Group) reduces the risk of fault reactivation in the Becancour area due to smaller fluid pressure build-up in simulations of series 2 (Fig. 7a). In simulations with high-reservoir permeability, shear slip along the Yamaska Fault, if occurs, happens later and over a shorter distance if compared to the simulations of series 1 (Fig. 7c). The Champlain Fault is reactivated in simulation with high reservoir permeability and high injection rate due to faster propagation of fluid flow toward the fault and fluid pressure build-up in the hanging wall. However, it is unlikely that high permeability of the reservoir units would be in reality constant over the distance of 4.4 km that separates the Champlain Fault and the injection well. The permeability of the reservoir units is mostly controlled by the presence of natural fractures, while the matrix permeability is low (Table 1). The natural fractures do not necessarily preserve the same density and orientation over the large distance, therefore the reservoir permeability might be variable and reactivation of the Champlain Fault is unlikely.

The present study confirms the previous results of reservoir-geomechanical simulations (Rutqvist et al., 2008) that the potential for shear failure along pre-existing fault is higher than the potential for tensile fracturing in caprock units. In simulations 2a-3a with medium injection rate, the effective minimum horizontal stress S_{xx}* above the injection zone remains negative after 30 years of injection indicating that no tensile fracturing would form (Fig. 12a-b), while the Yamaska Fault is already reactivated at 18-22 years (Figs 9-10). In simulation 4a with high injection rate, S_{xx}* becomes positive after 10 years of injection (Fig. 12c) meaning possible development of tensile fracturing of the intermediate units, while shear slip along the Yamaska fault occurred earlier, after 7.3 years of injection (Fig. 11b).

Our results suggest tensile fracturing might occur in relatively more rigid and brittle intermediate units (Beekmantown and Trenton Groups) starting in the most brittle rocks of the Theresa Formation and the Utica Shale above the injection zone (Fig. 12c; Table 1). However, it happens only after 10 years of continuous injection in the case of extremely high injection pressure (much higher than the minimum principal stress at the injection reservoir) as a result of high injection rate and low-reservoir permeability (run 4a, Table 5). Nevertheless, the thick (460 m) part of the caprock 2 unit (Lorraine Group) in this case remains intact for fracturing being located within the zone of negative (i.e. compressive) effective minimum horizontal stress. The risk of tensile fracturing under high injection rate is much lower if the reservoir units are characterized by higher reservoir permeability (Fig. 12d). The estimation of the risk of tension fracturing associated with injection-induced fluid pressure build-up likely represents the upper limit of tension fracturing predictions as the sandstones of aquifers 1 and 2 may have higher global permeability than applied in simulations due to the presence of natural fractures. Additional measurements would be necessary to evaluate the uncertainty related to capillary and entry pressure in the caprock units.

No tensile fracturing or fault shear slip occurs in the 2D Becancour model (Y=100 m) after 30 years of injection under the low-injection rate of 0.06 kg/s, which corresponds to the 3D injection rate of 4.5 kg/s (0.15 Mt/yr.) in a radial model (r=3300 m), i.e. pilot or small-scale CCS project. The simulation shows criterion for a sustainable (bottom-hole) injection pressure would be to keep it below the magnitude of the minimum principal stress at the depth of the reservoir, i.e. below 18 MPa for the depth of about 1 km as such an injection pressure would be unlikely to initiate reactivation. The similar conclusion was made after the estimation of regional stress magnitude (Konstantinovskaya et al., 2012). Moreover, even if reactivation is initiated the simulations show that it takes years of injection and further pressure build-up to reactivate a substantial rupture area that could propagate outside the injection zone and provide a leakage path.

Finally, the surface uplift above the injection zone in the case of low-injection rate (run 1) is small, varying from 1 cm to 2 cm at 30 years depending on the rock mass permeability of the reservoir units (Fig. 7b; Tables 5, 6). Higher injection rates result in higher surface uplift above the injection zone varying from 9 cm (runs 2-3) to 27.5 cm (run 4) after 30 years of continuous injection (Fig. 7b; Tables 4, 5). In simulations with the same injection rates but higher permeability of the aquifer units, the surface uplift is less pronounced (Fig. 7b; Table 6) for CO_2 plume propagates laterally further from the injection well along the aquifers 1 and 2 (Fig. 13d).

No CO_2 leakage after the fault reactivation can be expected in the Becancour area as the simulations results suggest. Even under high injection rates and long-term fault reactivation (runs 4a, 4b), the CO_2-saturated plume does not reach the Yamaska fault zone. The CO_2 plume lateral dimensions are up to 2 km in diameter maximum (Table 6) and it is forced to migrate away from the fault zone (Fig. 13) by asymmetric fluid-pressure build-up between the injection well and inclined fault plane (Fig. 6). The local fracturing of intermediate and caprock 1 units that started at 10 years of injection under high injection rates into the low-permeable reservoir units (Fig. 12c; Table 5) seems not to allow the upward migration of CO_2 plume, which remains trapped below tight intermediate units (Fig. 13c). Additionally, the caprock 2 units (Lorraine Group) would have prevented its upward migration for no throughout-caprock breach has been occurred in the experiments (Fig. 12). However, upward migration of brine along the Yamaska Fault might be expected in case of permeable fault behaviour and/or up-to-the surface fault-plane shear reactivation (runs 3a, 4a, 4b) under long-term high injection rates (Figs 10, 11, 14), similar to a putative storage site in the southern North Sea (Hannis et al., 2013). An understanding of brine flux along the fault as a migration pathway and environment impacts would need to be demonstrated in low-probable case of continuing CO2 injection after shear failure along the Yamaska Fault.

Further studies would be necessary to evaluate lateral changes of fault sealing capacity along the Yamaska fault to better understand the risk of fault reactivation and constrain the possible timing and localization of shear failure along the fault plane within a 3D model of the Becancour area. The along-strike variations in vertical offset and in orientation of fault plane relative to present-day stresses may cause lateral changes in permeability and in effective normal and shear stress acting on the fault plane that would influence the size of rupture area and, consequently, the magnitude of induced seismicity. 3D coupled reservoir-geomechanical TOUGH-FLAC modeling would be helpful to test strike-slip reactivation of the regional Yamaska and Champlain Faults under the regional strike-slip stress regime. 3D modeling will also allow us to obtain more realistic absolute values of injection rates that would be reasonable to apply without producing fault reactivation or caprock tensile fracturing.

The simulations with thermal option would be necessarily to carry out to better quantify temperature effects on the risk of the caprock breaching. After long-term CO_2 injection, temperature cooling effects can result in local reduction in the lateral stress around the injection well due to thermal contraction of the media, thus placing the overlying caprock in tensile stress (Gor et al., 2013), even though the far-field area thermally equilibrates with injected cold CO_2 (Vilarrasa et al., 2013). Indeed, significant changes in lateral stress associated with cold sea-water injection have been noted in the North Sea reservoirs (Dikken and Niko, 1987). The buoyancy-driven migration of CO_2 plume above the injection zone may reinforce the cooling effect of CO_2

injection contributing to the risk of caprock integrity. However, it was found that in stress regimes where the maximum principal stress is the vertical (as it is the case of the Becancour 2D model), thermal contraction induced by liquid CO_2 injection rather mobilizes shear slip along pre-existing fractures in the aquifer, while the mechanical stability of the caprock is improved (Vilarrasa et al., 2013).

5. CONCLUSIONS

The permeability of high-angle normal faults affecting the Early Paleozoic sedimentary succession of the St. Lawrence Lowlands basin is evaluated for the first time. The sealing capacity of the Champlain and the Yamaska Faults that bound the block targeted for CO_2 injection in the Becancour 2D model decreases with depth. The upper fault segments are characterized by shale gouge ratio (SGR) ranging from 17-21% to 95% and they are expected to behave as a seal. The lower fault segment of the Champlain Fault with SGR 7-11% might be permeable. However, the across-fault fluid flow along the low-SGR fault segment would be prevented by the presence of low-permeable rocks of the Grenvillian basement on the opposite side of the fault plane. The sample descriptions from the well A027, which penetrated the Yamaska Fault, and field observations of the Montmorency Fault confirm the fault planes with SGR > 17% are filled with thick continuous smears of calcareous shales similar to the caprock 1 unit (Utica Shale).

The coupled reservoir-geomechanical (TOUGH-FLAC) modeling of CO_2 injection tested at the Becancour 2D model confirms that injection may be carried out safely for at least 30 years with no shear or tensile failure to occur in the area if low injection rates and maximum injection pressure are respected. Our simulations indicate that the injection rate should be controlled such that the reservoir pressure is kept below the minimum compressive stress, which is about 18 MPa at reservoir depth (1 km).

The simulation results show that the likelihood of reactivating two reservoir-bounding faults (Yamaska and Champlain Faults) strongly depends on reservoir pressure at the faults, which in turn depends on injection rate, hydrological properties of aquifers and the distance between the faults and the injection well.

The fluid pressure build-up induced by injection is higher between the injection zone and the inclined Yamaska Fault due to close fault location (1.5 km) and sealing behaviour of the fault plane and the hanging wall. The fluid pressure increase is less significant toward the more distant

(4.4 km) Champlain Fault being distributed over larger area. Consequently, the CO_2 plume grows asymmetrically progressing toward the NW and away from the Yamaska Fault thus reducing the risk of CO_2 leakage along the fault plane.

Under high injection rate, the Yamaska Fault, which is located closer (1.5 km) to the injection zone has a higher potential to be reactivated than the more distant (4.4 km) Champlain Fault. The localization, timing, rate and length of shear slip along the Yamaska Fault depend on the initial fault permeability. A more permeable fault is reactivated earlier (after 18.2 years of injection) and shear failure is localized at the caprock level, within the segment (60 m) between the Utica Shale and Lorraine Group, progressing subsequently toward the surface. If the fault is a low permeability seal, fault slip occurs later (after 22.5 years of injection) and below the caprock units, along the segment (300 m) separating the intermediate units (Beekmantown-Trenton Groups) and the caprock 2 units (Lorraine Group). The shear slip progresses faster along a more permeable fault than along the fault with sealing behaviour.

High permeability of the reservoir units (Potsdam Group) results in smaller fluid pressure build-up due to more rapid fluid propagation away from the injection zone that reduces the risk of fault reactivation and tensile fracturing. The fault slip along the Yamaska Fault does not occur or it occurs later and the fault slip and surface uplift are less significant in simulations with high-reservoir permeability compared to the low-reservoir permeability runs. The propagation of fluid flow toward the Champlain Fault under the high-reservoir permeability settings triggers its reactivation after 30 years of injection, but it occurs only in the case of high injection rate.

The fluid pressure-induced tensile fracturing occurs above the injection zone only in the simulations with high injection rate, in which injection pressure becomes extremely high (much higher than minimum principal stress), and it happens long after shear failure of the Yamaska Fault. Tensile fractures are localized mostly within the more fragile intermediate units (Beekmantown and Trenton Groups) below the caprock system. The thick (460 m) part of the caprock 2 units (Lorraine Group) remains intact above the fractured zone preventing the upward migration of the injected CO_2.

ACKNOWLEDGMENTS

This study is supported by Ministère du Développement Durable, de l'Environnement, de la Faune et des Parc du Québec. It was carried out under the research collaborative project between INRS and LBNL, with funding for LBNL through the U.S. Department of Energy Contract No. DE-AC02-05CH11231. We are grateful to Associated Editor S. Bachu and two anonymous reviewers whose constructive comments and corrections of helped us to improve the original manuscript; Luc Massé and colleagues of Junex Inc. for cooperation and sharing the information on regional hydrological data.

REFERENCES

Agosta, F., Ruano, P., Rustichelli, A., Tondi, E., Galindo-Zaldívar, J., de Galdeano, C.S., 2012. Inner structure and deformation mechanisms of normal faults in conglomerates and carbonate grainstones (Granada Basin, Betic Cordillera, Spain): Inferences on fault permeability. J. Struct. Geol. 45, 4-20.

Arch, J., and Maltman, A., 1990. Anisotropic Permeability and Tortuosity in Deformed Wet Sediments. J. Geophys. Res. 95 (B6), 9035-9045.

Bachu, S., and Bennion, D.B., 2009. Interfacial tension between CO_2, freshwater, and brine in the range of pressure from (2 to 27) MPa, temperature from (20 to 125) °C, and water salinity from (0 to 334 000) mg*L^{-1}. J. Chem. Eng. Data 54 (3), 765-775.

Baranova, V., Mustaqeem, A., Bell, S., 1999. A model for induced seismicity caused by hydrocarbon production in the Western Canada Sedimentary Basin. Can. J. Earth Sci. 36, 47–64.

Barton, D. C., 2011. Determining CO_2 storage potential: characterization of seal Integrity and reservoir failure in exposed analogs. MS Thesis, Utah State University. 177 p.

Bennion, D.B., Bachu, S., 2008. Drainage and imbibition relative permeability relationships for supercritical CO_2/brine and H_2S/brine systems in intergranular sandstone, carbonate, shale, and annhydrite rocks. SPE Reservoir Evaluation & Engineering 11, 487–496.

Berry, M.J., and Hasegawa, H.S., 1979. Seismic risk and toxic waste disposal: a discussion. Geoscience Canada 6(4), 195-198.

Burton, M., Kumar, N., Bryant, S.L., 2009. CO_2 injectivity into brine aquifers: why relative permeability matters asmuchas absolute permeability. Energy Procedia 1, 3091–3098.

Busch, A., and Amann-Hildebrand, A., 2013. Predicting capillarity of mudrocks. Marine and Petroleum Geology 45, 208-223.Cappa, F., and Rutqvist, J., 2011a. Impact of CO_2 geological sequestration on the nucleation of earthquakes. Geophys. Res. Letters 38, L17313, doi: 10.1029/2011GL048487

Cappa, F., and Rutqvist, J., 2011b. Modeling of coupled deformation and permeability evolution during fault reactivation induced by deep underground injection of CO_2. Int. J. Greenhouse Gas Control 5, 336–346.

Cappa, F., and Rutqvist, J., 2012. Seismic rupture and ground accelerations induced by CO_2 injection at shallow crust. Geophys. J. Int. 190, 1784-1789.

Carles, P., Bachaud, P., Lasseur, E., Berne, P., Bretonnier, P. 2010. Confining properties of carbonated Dogger caprocks (Parisian Basin) for CO_2 storage purpose. Oil & Gas Sci and Technol – Rev IFP 65, 461–472.

Castonguay, S., Dietrich, J., Lavoie, D., Laliberté, J-Y., 2010. Structure and petroleum plays of the St. Lawrence Platform and Appalachians in southern Quebec: insights from interpretations of MRNQ seismic reflection data. Bull. Can. Petrol. Geol. 58 (3), 219-234.

Chadwick, A., Arts, R., Bernstone, C., May, F., Thibeau, S., Zweigel, P., 2008. Best practice for the storage of CO_2 in saline aquifers: Observations and guidelines from the SACS and CO2STORE projects. Keyworth, Nottingham, British Geological Survey.

Chang, K., Bryant, S.L., 2008. The effect of faults on dynamics of CO_2 plumes: presented at the 9th International Conference on Greenhouse Gas Control Technologies (GHGT-9), Washington, D.C., November 16-20, 2008. GCCC Digital Publication Series #08-03b.

Chiaramonte, L., Zoback, M. D., Friedmann, J., Stamp, V., 2008. Seal integrity and feasibility of CO_2 sequestration in the Teapot Dome EOR pilot: geomechanical site characterization. Environ Geol 54, 1667–1675.

Claprood, M., Gloaguen, E., Giroux, B., Duchesne, M.J., Konstantinovskaya, E., Malo, M., 2012. Workflow using sparse vintage data for building a first geological and reservoir model for CO_2 storage in deep saline aquifer. A case study in the St. Lawrence Platform, Canada. Greenhouse Gas Sci. Technol. 2, 1-19. doi:10.1002/ghg.1292

Committee on Induced Seismicity Potential in Energy Technologies, Induced Seismicity Potential in Energy Technologies, National Research Council, Washington, DC, 2012. http://dels.nas.edu/ Report/Induced-Seismicity-Potential-Energy-Technologies/13355

Corey, A.T., 1954. The interrelation between oil and gas relative permeabilities. Producers Monthly, 19 (1), 38–41.

Coussy, O., 2004. Poromechanics. John Wiley and Sons: Chichester, England. 298 p.

Davies, R., Foulger, G., Bindley, A., Styles P., 2013. Induced seismicity and hydraulic fracturing for the recovery of hydrocarbons. Marine Petrol. Geol. 45, 171-185.

Dikken, B.J., and Niko, H., 1987. Waterflood-induced fractures: a simulation study of their propagation and effects on waterflood sweep efficiency. Proc. SPE Conf. Offshore Europe, 8-11 September 1987, Aberdeen, United Kingdom, 15 p, SPE#16551-MS

Doveton, J.H., 1986. Log analysis of subsurface geology: concepts and computer methods. John Wiley and Sons, Inc. 273 p.

Ellsworth, W.L., 2013. Injection-Induced Earthquakes. Science. 341, 1225942. doi: 10.1126/ science.1225942

Farish, L. M., 1933. Report on the geology of the Ste. Angele No. 1 well and recommendations for the drilling of a second well including estimated cost analysis. Ministère des Richesses Naturelles, Québec, No. 4983.

Freeman, B., Yielding, G., Needham, D. T., Badley, M. E., 1998. Fault seal prediction: the gouge ratio method, in: Coward, M. P., Daltaban, T. S. Johnson, H. (Eds.), Structural Geology in Reservoir Characterization. Geol. Society, London, Spec. Publ. 127, pp. 19-25.

GCCSI, 2012. Global CCS Institute: The Global Status of CCS. 228 p. Available at http://www.globalccsinstitute.com/publications/global-status-ccs-2012 (accessed 03-09-2013).

Gor, G.Yu., Elliot, T.R., Prévost, J.H., 2013. Effects of thermal stresses on caprock integrity during CO_2 storage. Int. J. Greenhouse Gas Control 12, 300-309.

Globensky, Y., 1987. Géologie des Basses-Terres du Saint-705 Laurent : Québec. Ministère de l'Énergie et des Ressources. MM 85-02. 63 p.

Hannis, S. D.; Bricker, S.; Williams, J.D.O., 2013. Effects of faults as barriers or conduits to displaced brine flow on a putative CO_2 storage site in the Southern North Sea. EGU General Assembly 2013, held 7-12 April, 2013 in Vienna, Austria, id. EGU2013-9491

Hawkes, C.D., McLellan, P.J., Bachu, S., 2005. Geomechanical factors affecting geological storage of CO_2 in depleted oil and gas reservoirs. J. Can. Petrol. Technol. 44, 52–61.

Healy, J.H., Rubey, W.W., Griggs, D.T., Raleigh, C.B., 1968. The Denver earthquakes. Science 161 (3848), 1301–1310.

Hildenbrand, A., Schlomer, S., Kroos, M.K., 2004. Gas breakthrough experiments on pelitic rocks: comparative study with N2, CO_2 and CH_4, Geofluids 2, 61–80.

Hsieh, P.A., and Bredehoeft, J.D., 1981. A reservoir analysis of the Denver earthquakes: A case of induced seismicity. J. Geophys. Res. 86 (2), 903–920.

Itasca Consulting Group, 2009. FLAC3D, Fast Lagrangian Analysis of Continua in 3 Dimensions. Version 4.0. Twelve volumes. Itasca Consulting Group, Minneapolis, MN.

Jordan, P.D., Oldenburg, C.M., Nicot, J.-P., 2013. Measuring and modeling fault density for CO_2 storage plume-fault encounter probability estimation, AAPG Bulletin 97 (4), 597-618.

Konstantinovskaya, E.A., Rodriguez, D., Kirkwood, D., Harris, L.B., Thériault, R., 2009. Effects of basement structure, sedimentation and erosion on thrust wedge geometry: an example from the Quebec Appalachians and analogue models. Bull. Can. Petrol. Geol. 57 (1), 34–62.

Konstantinovskaya, E., Malo, M., Castillo, D.A., 2012. Present-day stress analysis of the St. Lawrence Lowlands sedimentary basin (Canada) and implications for caprock integrity during CO_2 injection operations. Tectonophysics 518, 119-137. doi:10.1016/j.tecto.2011.11.022

Lucier, A., Zoback, M., Gupta, N., Ramakrishnan, T. S., 2006. Geomechanical aspects of CO_2 sequestration in a deep saline reservoir in the Ohio River Valley region. Environ. Geosci. 13 (2), 85–103.

Malo, M., and Bédard, K., 2012. Basin-Scale Assessment for CO_2 Storage Prospectivity in the Province of Québec, Canada. Energy Procedia 23, 487 – 494.

Massé, L., 2009. Geological storage in Quebec. 1er colloque de la Chaire en séquestration géologique du CO_2. La technologie du CSC au Québec: Qui sont les acteurs, Québec, 20 Avril 2009. http://chaireco2.ete.inrs.ca/sites/chaireco2.ete.inrs.ca/files/Junex_CSC_Quebec_20-04-09.pdf

Mathias, S.A., Gonzalez, G.J., Thatcher, K.E., Zimmerman, R.W., 2011a. Pressure buildup during CO_2 injection into a closed brine aquifer. Transport in Porous Media 89 (3), 383–397.

Mathias, S.A., Gluyas, J.G., Gonzalez Martinez de Miguel, G.J., Hosseini, S.A., 2011b. Role of partial miscibility on pressure buildup due to injection of CO_2 into closed and open brine aquifers. Water Resources Research 47, W12525.

Mathias, S. A., Gluyasa, J. G., González Martínez de Miguel, G. J., Bryant, S. L., Wilson, D., 2013. On relative permeability data uncertainty and CO_2 injectivity estimation for brine aquifers. Int. J. Greenhouse Gas Control 12, 200-212.

Mathieson, A., Midgley, J., Dodds, K., Wright, I., Ringrose, P., Saoul, N., 2010. CO_2 sequestration monitoring and verification technologies applied at Krechba, Algeria. Lead Edge 29, 216–222

Mathieson, A., Midgley, J., Wright, I., Saoul, N., Ringrose, P., 2011. In Salah CO_2 Storage JIP: CO_2 sequestration monitoring and verification technologies applied at Krechba, Algeria. Energy Procedia 4, 3596–3603

Mazzoldi, A., Rinaldi, A.P., Borgia, A., and Rutqvist, J., 2012. Induced seismicity within geological carbon sequestration projects: Maximum earthquake magnitude and leakage potential, Int. J. Greenhouse Gas Control 10, 434-442.

McClain, W.C., 1970. On earthquakes produced by underground fluid injection. Oak Ridge Natl. Lab., Tenn., ORNL-TM-3154.

Miller, S.A., Collettini, C., Chiaraluce, L., Cocco, M., Barchi, M., Kaus, B.J.P., 2004. Aftershocks driven by a high-pressure CO_2 source at depth. Nature 427, 724–727.

Milne, W.G. 1970. The Snipe Lake, Alberta, earthquake of March 8, 1970. Can. J. Earth Sci. 6, 1564–1567

Murphy, S., O'Brien, G. S., McCloskey, J., Bean, C. J., Nalbant, S., 2013. Modelling fluid induced seismicity on a nearby active fault. Geophys. J. Int. 194, 1613–1624.

NETL. 2013. Carbon Sequestration FAQ Information Portal: Permanence and Safety of CCS. Available at www.netl.doe.gov/technologies/carbon_seq/FAQs/permanence2.html (accessed September 3, 2013)

Nicol, A., Carne, R., Gerstenberger, M., Christophersen, A., 2011. Induced seismicity and its implications for CO_2 storage risk. Energy Procedia 4, 3699–3706

Onuma, T, Ohkawa, S., 2009. Detection of surface deformation related to CO_2 injection by DInSAR at In Salah, Algeria. Energy Procedia 1, 2177-2184.

Raleigh, C. B. Healy, J. H. Bredehoeft, J. D., 1976. An Experiment in Earthquake Control at Rangely, Colorado. Science 191, 1230-1237.

Rinaldi, A. P., and Rutqvist, J., 2013. Modeling of deep fracture zone opening and transient ground surface uplift at KB-502 CO_2 injection well, In Salah, Algeria. Int. J. Greenhouse Gas Control 12, 155–167.

Rutqvist, J., 2011. Status of TOUGH-FLAC simulator and recent applications related to coupled fluid flow and crustal deformations. Computers Geosci. 37, 739-750.

Rutqvist, J., 2012. The Geomechanics of CO_2 Storage in Deep Sedimentary Formations. Geotech. Geol. Eng. DOI 10.1007/s10706-011-9491-0

Rutqvist, J., Birkholzer, J.T., Tsang, C.-F., 2008. Coupled reservoir-geomechanical analysis of the potential for tensile and shear failure associated with CO_2 injection in multilayered reservoir-caprock systems. Int. J. Rock Mech. Min. Sci. 45, 132–143.

Shemeta, J. E., Eide, E. A., Hitzman, M. W., Clarke, D. D., Detournay, E., Dieterich, J. H., Dillon, D. K., Green, S. J., Habiger, R. M., McGuire, R. K., Mitchell, J. K., Smith, J. L., Ortego, J. R., Gibbs, C. R., 2012. The potential for induced seismicity in energy technologies. The Leading Edge 31, 1438-1444.

Sibson, R.H., 1992. Implications of fault-valve behavior for rupture nucleation and recurrence. Tectonophysics 211, 283–293.

Song, J., and Zhang, D., 2013. Comprehensive Review of Caprock-Sealing Mechanisms for Geologic Carbon Sequestration. Environ. Sci. Technol. 47, 9−22.

Streit, J.E., and Cox, S.F., 2001. Fluid pressures at hypocenters of moderate to large earthquakes. J. Geophys. Res. 106, 2235–2243.

Streit, J.E., and Hillis, R.R., 2004. Estimating fault stability and sustainable fluid pressures for underground storage of CO_2 in porous rock. Energy 29, 1445–1456.

Suckale, J., 2010. Moderate-to-large seismicity induced by hydrocarbon production. The Leading Edge 29, 310-319.

Thériault, R., Laliberté, J.-Y., Brisebois, D., et Rheault, M., 2005. Fingerprinting of the Ottawa–Bonnechère and Saguenay grabens under the Saint-Lawrence Lowlands and Quebec Appalachians: prime targets for hydrocarbon exploration. Geol. Ass. Can., Abstracts. Halifax, Nova Scotia, 65.

Tran Ngoc, T.D., Lefebvre, R., Malo, M., Doughty, C., 2012. Feasibility of CO_2 injection in the deep saline aquifers of the Bécancour region, Québec (Canada), in: Finsterle, S., Hawkes, D., Moridis, G. (Eds.), TOUGH Symposium, Berkeley, Calif., 17-19 September 2012, pp. 757-766.

van Genuchten, M.T., 1980. A closed-form equation for predicting the hydraulic conductivity of unsaturated soils. Soil Sci. Soc. Am. J. 44, 892–898.

Vidal-Gilbert, S., Tenthorey, E., Dewhurst, D., Ennis-King, J., Van Ruth, P., Hillis, R., 2010. Geomechanical analysis of the Naylor Field, Otway Basin, Australia: implications for CO_2 injection and storage. Int. J. Greenhouse Gas Control 4:827–839.

Vilarrasa, V., Silva, O., Carrera, J., Olivella, S., 2013. Liquid CO_2 injection for geological storage in deep saline aquifers. Int. J. Greenhouse Gas Control 14, 84-96.

Wyss, M. and Molnar, P. 1972. Efficiency, stress drop, apparent stress, effective stress, and frictional stress of Denver, Colorado, earthquakes. J. Geophys. Res. 77(8), 1433–1438

Yielding, G., Freeman, B., and Needham, D. T., 1997. Quantitative Fault Seal Prediction. AAPG Bull. 81 (6), 897–917.

Zhang, Y., Person, M., Rupp, J., Ellett, K., Celia, M. A., Gable, C. W., Bowen, B., Evans, J., Bandilla, K., Mozley, P., Dewers, Th., Elliot, Th., 2013. Hydrogeologic controls on induced seismicity in crystalline basement rocks due to fluid injection into basal reservoirs. Groundwater 51 (4), 525–538.

Zoback, M.D., 2010. Reservoir geomechanics. Cambridge University Press, New York, 449 p.

Zoback, M. D., and Gorelick, S. M., 2012. Earthquake triggering and large-scale geologic storage of carbon dioxide. PNAS. 5 p. www.pnas.org/cgi/doi/10.1073/pnas.1202473109

FIGURE CAPTIONS

Fig. 1. Geological map of the St. Lawrence Lowlands modified after Globensky (1987) and Konstantinovskaya et al. (2009; 2012). Stratigraphic units: 1, siliciclastic units of the Queenston, Lorraine Groups and Lotbinière Formation, 2, Utica Shale, 3, carbonates of the Trenton, Black River and Chazy Groups, 4, dolomites and sandstones of the Beekmantown Group, 5, sandstones of the Potsdam Group; 6, thrust; 7, normal fault at surface; 8, normal fault at top of the Grenvillian basement (after Thériault et al., 2005); 9, fault observation station. S_{Hmax} orientation is shown after Konstantinovskaya et al. (2012a). The numbers along the normal faults indicate vertical offset in meters, after Globensky (1987) and references therein and author's data. The cross-sections are simplified after interpreted seismic lines from Castonguay et al. (2010); vertical scale is given in seconds, two-way traveltime (TWT, s). Fault abbreviations: JF, Joliette; SCF, Saint-Cuthbert; SPF, Saint-Prosper; SA, Saint-Albin; DF, Deschambault; JCF, Jacques-Cartier; NF, Neuville; MF, Montmorency; CTF, Cap-Tormente; ChF, Chamlplain; YF, Yamaska; AF, Aston; LL, Logan's Line. *TR*, Trois-Rivières; *Bc*, Becancour.

Fig. 2. Time structure of the Grenvillian basement in the Becancour area, modified after Thériault et al. (2005). Contour lines of the basement elevation are given in milliseconds, two-way traveltime (TWT, ms). The well numbers are given after the MRNF database (see Appendix). See Fig. 1 for the map location.

Fig. 3. The 2D geological model of the Becancour area used in the reservoir-geomechanical modeling. See Fig. 2 for the cross-section location. Note that for simplicity the normal faults in the model are traced up to the surface; although seismic data support the continuation of faults occurs only up to the top of the Utica Shale (see Fig. 1, cross-sections).

Fig. 4 Cross-section of the Montmorency Fault (a) and photograph of the fault zone (b). The box on the cross-section indicates the location of the photograph. See Fig. 1 for the cross-section location.

Fig. 5. The simplified 2D cross-sections used for estimation of shale-gouge ratio (SGR) for the Champlain (a) and the Yamaska (b) Faults. Numbers along the fault planes indicate the obtained SGR values. Tops and thickness of stratigraphic units presented in the cross-sections (Table 3) are

interpreted from regional well log data, 2D model (Fig. 3) and 3D geological model of the Becancour area (Claprood et al., 2012). CH* indicates reservoir sandstones of the Covey Hill Formation (aquifer 1) targeted for CO_2 injection. See more explanation in the text.

Fig. 6. Fluid pressure variations occurred in the reservoir and intermediate units after 30 years of injection in simulations with low (a) and high (b) reservoir permeability. See Table 4 for initial parameters. Abbreviations: GB, Grenvillian basement; aq, aquifer; int, intermediate; cp, caprock units; see Fig. 3 for their stratigraphic analogs.

Fig. 7. Changes in fluid pressure (a), vertical surface uplift above the injection zone (b), fault slip (c) and effective shear strain increment (d) as a function of time occurred in the injection zone (well) and along the Yamaska Fault (fault zone) in simulations of series 1 (1a-4a) and series 2 (1b-4b). See Table 4 for initial and Tables 5 and 6 for resulting parameters. S_{xx}* is effective minimum horizontal stress.

Fig. 8. Changes in effective shear strain occurred around the injection zone and along the Yamaska Fault during subsequent steps of run 1a, injection rate 0.06 kg/s, sealing fault behaviour. No fault reactivation occurs in this simulation. See Table 4 for initial and Table 5 for resulting parameters. See Fig. 6 for abbreviation symbols.

Fig. 9. Changes in effective shear strain occurred around the injection zone and along the Yamaska Fault during subsequent steps of run 2a, injection rate 0.3 kg/s, sealing fault behaviour. Fault slip occurs after 22.5 years of injection, within the segment separating the intermediate and caprock 2 units (b). Afterward, the shear strain increment diminishes in the injection zone and deformation localizes mostly along the fault zone (c-d), remaining within the fault segment below the caprock 2 units. See Table 4 for initial and Table 5 for resulting parameters. See Fig. 6 for abbreviation symbols.

Fig. 10. Changes in effective shear strain occurred around the injection zone and along the Yamaska Fault during subsequent steps of run 3a, injection rate 0.3 kg/s, permeable fault behaviour. Fault slip occurs after 18.2 years of injection (b) in the segment separating the caprock 1 and caprock 2 units. Afterward, the shear strain localizes along the fault and fault slip propagates toward the surface (c-d). See Table 4 for initial and Table 5 for resulting parameters. See Fig. 6 for abbreviation symbols.

Fig. 11. Changes in effective shear strain occurred around the injection zone and along the Yamaska Fault during subsequent steps of run 4a, injection rate 1 kg/s, sealing fault behaviour. Fault slip occurs after 7.3 years of injection (b) in the segment separating the intermediate and caprock 2 units. Afterward, the shear strain localizes along the fault and fault slip propagates up the surface (c-d). See Table 4 for initial and Table 5 for resulting parameters. See Fig. 6 for abbreviation symbols.

Fig. 12. The fluid-pressure induced changes in effective minimum horizontal stress S_{xx}* occurred above the injection zone in simulations of series 1 (a-c) and 2 (d) after 30 (a-b) and 17.9-17.8 (c-d) years of injection. Negative (i.e. compressive) S_{xx}* indicates tensile fracturing is unlikely to form (a, b); zones of positive S_{xx}* (P_f>S_{xx}) correspond to the settings favorable for tensile fracturing (c, d). The large zone of positive S_{xx}* occurs in run 4a (c) under high injection rate within the intermediate units but the thick part (460 m) of the caprock 2 units still remains intact. See Table 4 for initial and Tables 5 and 6 for resulting parameters. See Fig. 6 for abbreviation symbols.

Fig. 13. Changes in liquid saturation S_L and geometry of CO_2 plume (cold colors) in the injection zone after 30 years of injection. The dotted lines indicate CO_2 plume geometry observed in runs of series 2 compared to runs of series 1 (a, b), or during the progressive steps within the same runs (c, d). Note the progressive growth of CO_2 plume away from the Yamaska Fault (c, d). See Table 4 for initial and Tables 5 and 6 for resulting parameters. See Fig. 6 for abbreviation symbols.

Fig. 14. Changes in effective shear strain occurred around the injection zone and along the Champlain and the Yamaska Faults during subsequent steps of run 4b, injection rate 1 kg/s, sealing fault behaviour. The Yamaska Fault is reactivated after 7.8 years of injection (a) in the segment separating the intermediate and caprock 2 units. Afterward, the shear strain localizes along the Yamaska fault and fault slip propagates up the surface (b-d). The Champlain Fault is reactivated after 30 years of injection (d) within the segment separating the targeted reservoir units of aquifer 1 and the Grenvillian basement. See Table 4 for initial and Table 6 for resulting parameters. See Fig. 6 for abbreviation symbols.

TABLES

Table 1. Main representative properties of Lower Paleozoic sedimentary units in the Becancour area.

Note: The elastic properties E, ν, porosity and matrix permeability data are obtained from laboratory core analyses; λ, K, and G are calculated from E and ν, after (Zoback, 2010); [a], determined from drill stem tests (Tran Ngoc et al., 2012); *k* vertical = 0.1 x *k* horizontal; [b], spacing between joints. Elastic moduli for the Grenvillian basement are taken as an average granite value; for the Trenton-Black River-Chazy Groups - as equal to the Beauharnois Fm; the data on fluid-property parameters (salinity, saturation, capillary pressure and compressibility) are taken from Tran Ngoc et al. (2012).

Table 2. Changes of stress/pressure and temperature with depth in the Becancour area

Table 3. Estimation of seal capacity for the Champlain and the Yamaska Faults using the shale gouge ratio method (Freeman et al., 1998; Yielding et al., 1997).

Note: V_{sh}, volume of shale estimated from natural radioactivity (gamma ray) well log data; Z, depth of formation tops estimated for the Yamaska Fault as an average value from the 3D geological model of the Becancour area (Claprood et al., 2012) and for the Champlain Fault from correlation of regional well data and basement top (Fig. 3). FW, footwall, HW, hanging wall.

Table 4. Initial parameters used in numerical simulations.

Note: CH, Covey Hill Fm; Ca, Cairnside Fm.; k_1, k_2, rock mass permeability; k_m, matrix permeability.

Table 5. Resulting variations in fluid pressure build-up (ΔP_f), effective shear strain increment ($\Delta\gamma$), surface uplift (h), length of reactivated fault segment (L), maximum fault shear slip (d), effective minimum horizontal stress (S_{xx}*) and CO_2 plume width (W) observed in numerical simulations 1a-4a of series 1 ($k_1 = 10k_m$) for different injection rates (IR) and fault permeability (k_f).

Note: YF, Yamaska Fault; FW unit, footwall unit: CH, Covey Hill Fm; Ca, Cairnside Fm; th, Theresa Fm; Tr, Trenton Group; Ut, Utica Shale; Lor, Lorraine Group. See Table 4 for the rock mass k_1 and matrix k_m permeability of the reservoir units.

Table 6. Resulting variations in fluid pressure build-up (ΔP_f), effective shear strain increment ($\Delta\gamma$), surface uplift (h), length of reactivated fault segment (L), maximum fault shear slip (d), effective minimum horizontal stress (S_{xx}*) and CO_2 plume width (W) observed in numerical simulations 1b-4b of series 2 ($k_2 = 100k_m$) for different injection rates (IR) and fault permeability (k_f).

Note: YF, Yamaska Fault; [a], reactivation of the Champlain Fault; FW unit, footwall unit: GB, Grenvillian basement; CH, Covey Hill Fm; Ca, Cairnside Fm; th, Theresa Fm; Tr, Trenton Group; Ut, Utica Shale; Lor, Lorraine Group. See Table 4 for the rock mass k_2 and matrix k_m permeability of the reservoir units.

Appendix. Name and location of wells in the St. Lawrence Lowlands cited in present study. See Fig. 2 for well location.

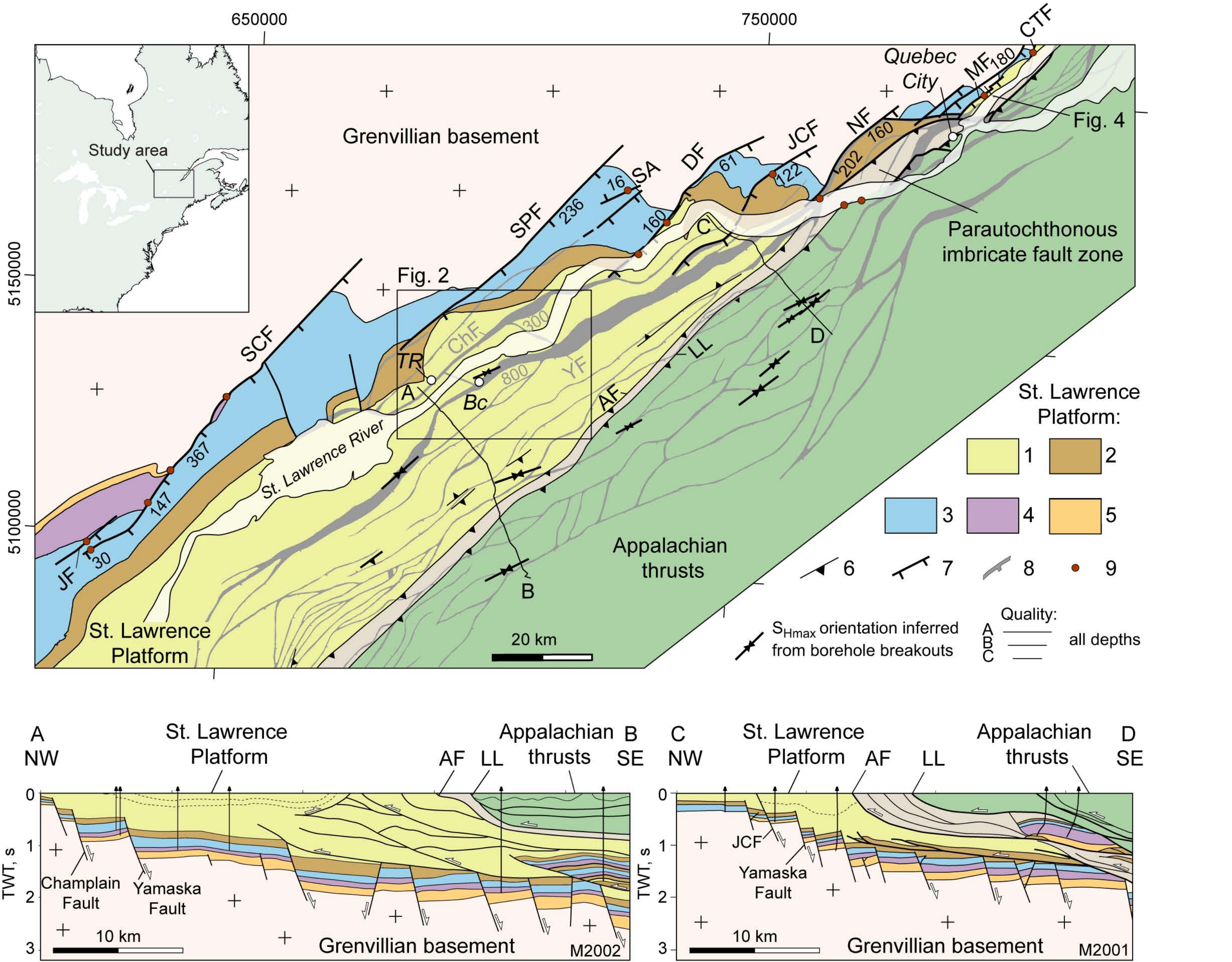
650000
750000
5150000
5100000
Study area
Grenvillian basement
Quebec City
Fig. 4
Fig. 2
CTF
MF
NF
JCF
DF
SA
SPF
SCF
JF
ChF
YF
TR
Bc
AF
LL
St. Lawrence River
Parautochthonous imbricate fault zone
St. Lawrence Platform
Appalachian thrusts
St. Lawrence Platform:
1
2
3
4
5
6
7
8
9
20 km
S_{Hmax} orientation inferred from borehole breakouts
Quality:
A
B
C
all depths
A
NW
St. Lawrence Platform
Appalachian thrusts
B
SE
AF
LL
Champlain Fault
Yamaska Fault
Grenvillian basement
TWT, s
10 km
M2002
C
NW
D
SE
JCF
Yamaska Fault
M2001

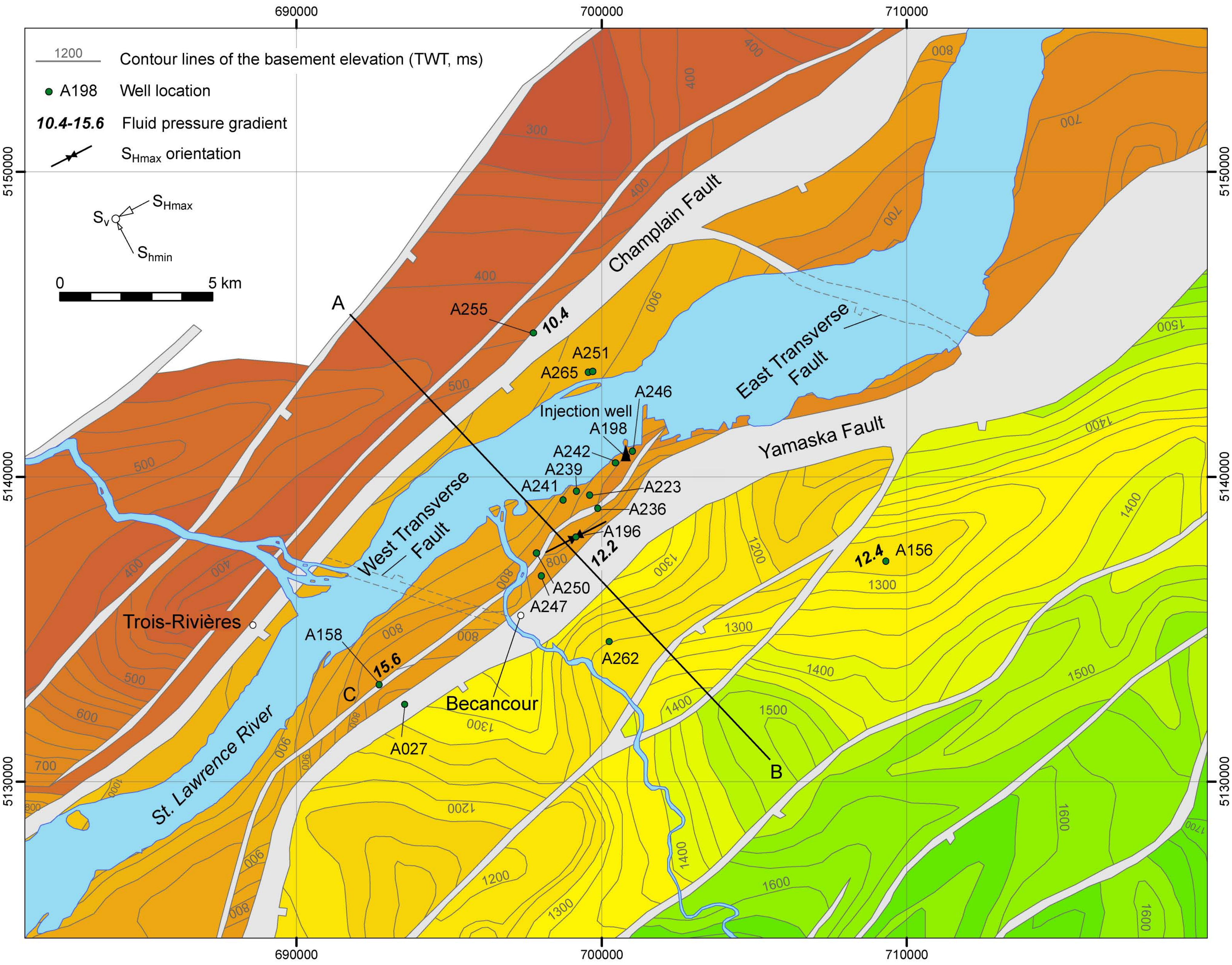
690000
700000
710000
5150000
5140000
5130000
1200 Contour lines of the basement elevation (TWT, ms)
A198 Well location
10.4-15.6 Fluid pressure gradient
S_{Hmax} orientation
S_v
S_{Hmax}
S_{hmin}
0
5 km
Champlain Fault
East Transverse Fault
Yamaska Fault
West Transverse Fault
St. Lawrence River
Trois-Rivières
Becancour
Injection well
A
B
C
A255
10.4
A251
A265
A246
A198
A242
A239
A241
A223
A236
A196
12.2
A250
A247
A158
15.6
A027
A262
12.4
A156

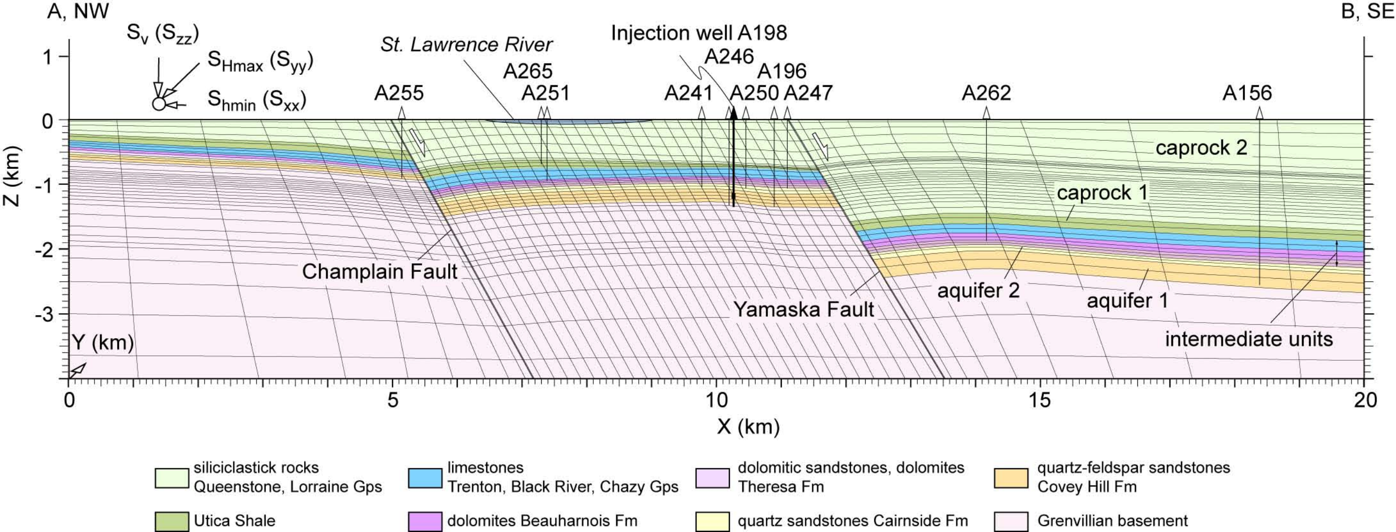

A, NW
B, SE
S_v (S_{zz})
S_{Hmax} (S_{yy})
S_{hmin} (S_{xx})
St. Lawrence River
Injection well A198
A246
A265
A196
A255
A251
A241
A250
A247
A262
A156
caprock 2
caprock 1
Champlain Fault
Yamaska Fault
aquifer 2
aquifer 1
intermediate units
Y (km)
Z (km)
X (km)
siliciclastick rocks Queenstone, Lorraine Gps
limestones Trenton, Black River, Chazy Gps
dolomitic sandstones, dolomites Theresa Fm
quartz-feldspar sandstones Covey Hill Fm
Utica Shale
dolomites Beauharnois Fm
quartz sandstones Cairnside Fm
Grenvillian basement

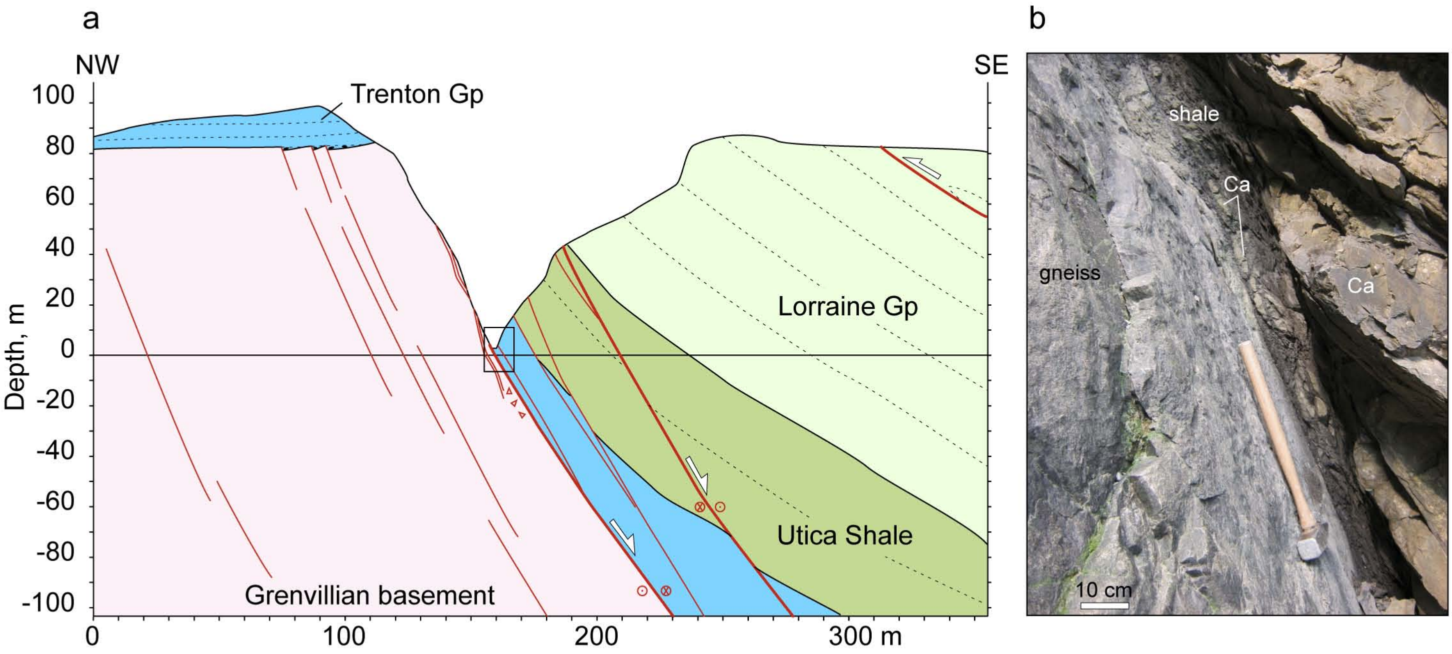
a
b
NW
SE
Trenton Gp
Lorraine Gp
Utica Shale
Grenvillian basement
Depth, m
100
80
60
40
20
0
-20
-40
-60
-80
-100
0
100
200
300 m
shale
Ca
gneiss
Ca
10 cm

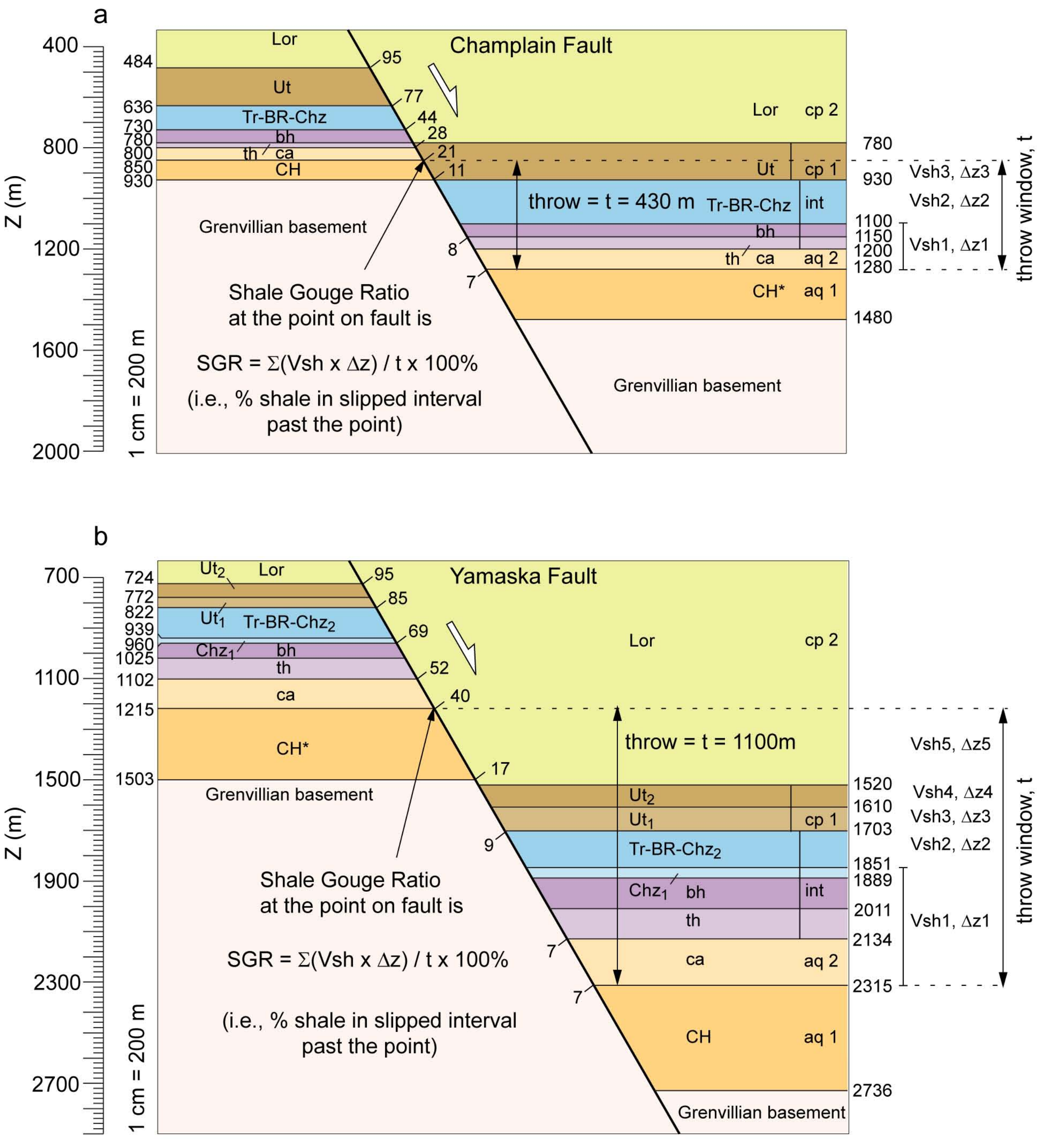

a
Champlain Fault
Lor
Ut
Tr-BR-Chz
bh
th
ca
CH
Grenvillian basement
Lor
cp 2
Ut
cp 1
Tr-BR-Chz
int
bh
th
ca
aq 2
CH*
aq 1
Grenvillian basement
throw = t = 430 m
95
77
44
28
21
11
8
7
484
636
730
780
800
850
930
780
930
1100
1150
1200
1280
1480
Vsh3, Δz3
Vsh2, Δz2
Vsh1, Δz1
throw window, t
Shale Gouge Ratio
at the point on fault is
SGR = Σ(Vsh x Δz) / t x 100%
(i.e., % shale in slipped interval
past the point)
Z (m)
400
800
1200
1600
2000
1 cm = 200 m
b
Yamaska Fault
Ut2
Lor
Ut1
Tr-BR-Chz2
Chz1
bh
th
ca
CH*
Grenvillian basement
Lor
cp 2
Ut2
Ut1
cp 1
Tr-BR-Chz2
Chz1
bh
int
th
ca
aq 2
CH
aq 1
Grenvillian basement
throw = t = 1100m
95
85
69
52
40
17
9
7
7
724
772
822
939
960
1025
1102
1215
1503
1520
1610
1703
1851
1889
2011
2134
2315
2736
Vsh5, Δz5
Vsh4, Δz4
Vsh3, Δz3
Vsh2, Δz2
Vsh1, Δz1
throw window, t
Shale Gouge Ratio
at the point on fault is
SGR = Σ(Vsh x Δz) / t x 100%
(i.e., % shale in slipped interval
past the point)
Z (m)
700
1100
1500
1900
2300
2700
1 cm = 200 m

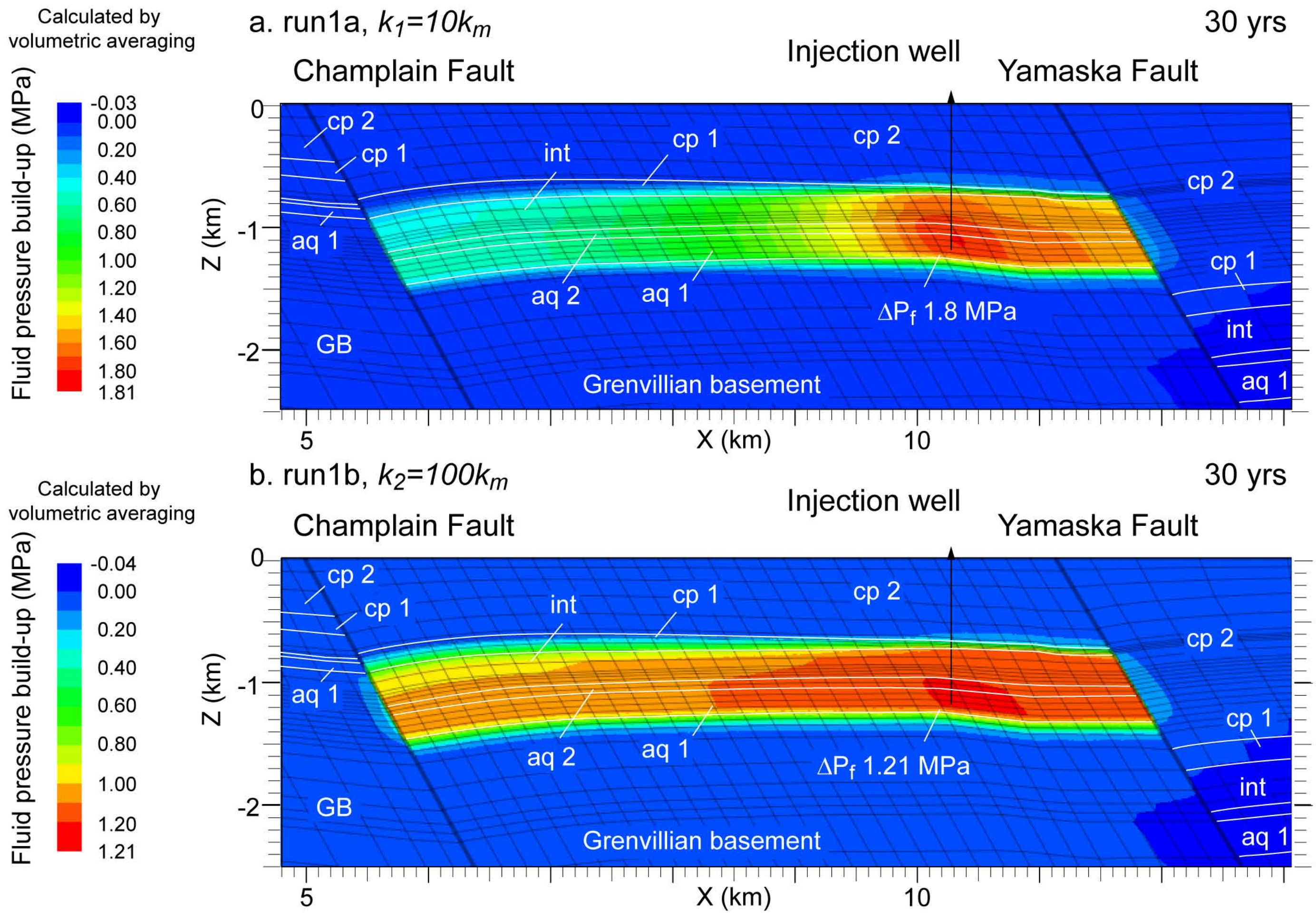

a. run1a, $k_1=10k_m$
30 yrs
Calculated by volumetric averaging
Fluid pressure build-up (MPa)
-0.03
0.00
0.20
0.40
0.60
0.80
1.00
1.20
1.40
1.60
1.80
1.81
Injection well
Champlain Fault
Yamaska Fault
cp 2
cp 1
int
aq 1
aq 2
GB
Grenvillian basement
ΔP_f 1.8 MPa
Z (km)
0
-1
-2
X (km)
5
10
b. run1b, $k_2=100k_m$
30 yrs
Calculated by volumetric averaging
Fluid pressure build-up (MPa)
-0.04
0.00
0.20
0.40
0.60
0.80
1.00
1.20
1.21
Injection well
Champlain Fault
Yamaska Fault
ΔP_f 1.21 MPa
Grenvillian basement

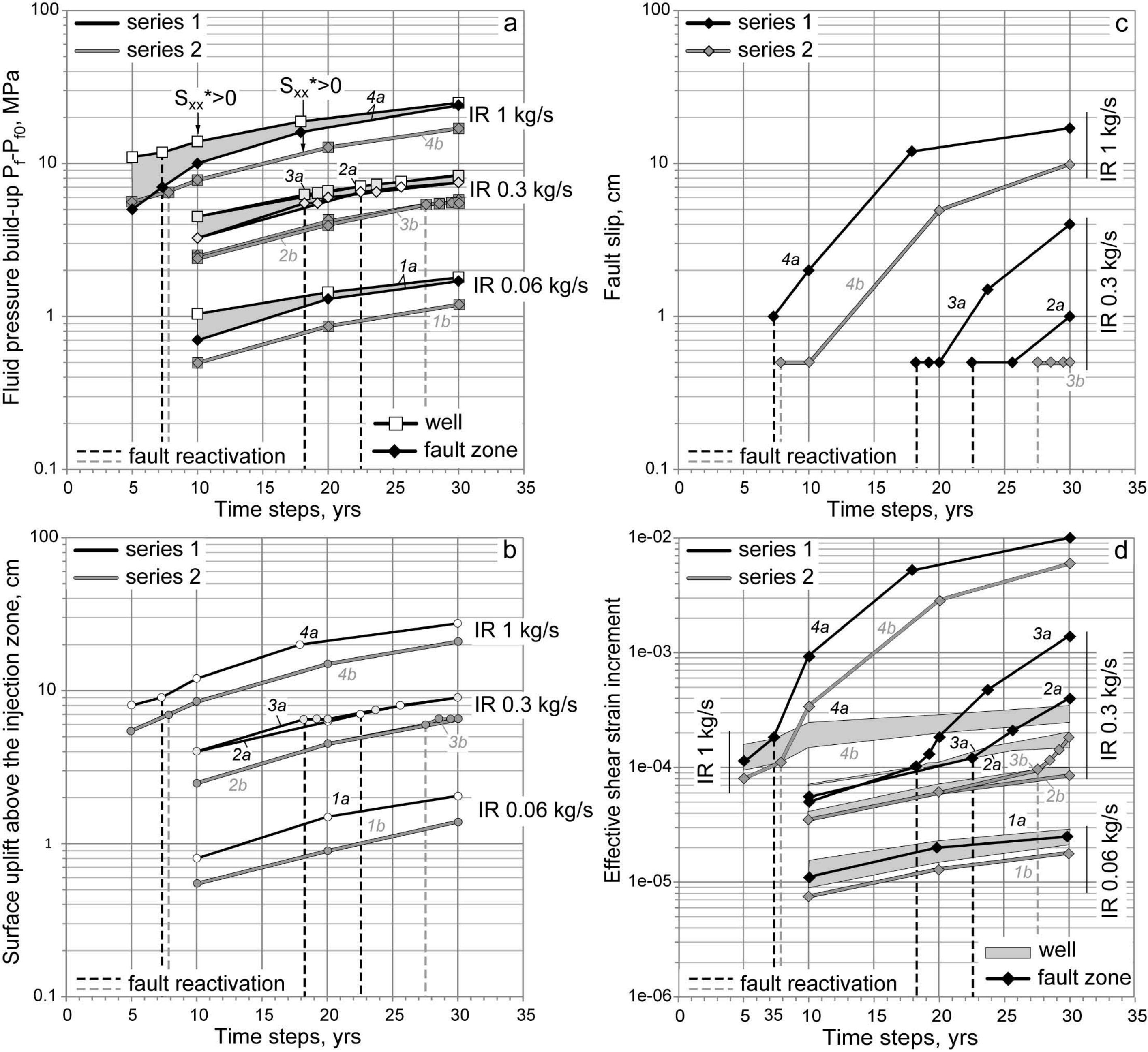

a
series 1
series 2
Fluid pressure build-up P_f-P_{f0}, MPa
S_{xx}*>0
S_{xx}*>0
IR 1 kg/s
IR 0.3 kg/s
IR 0.06 kg/s
4a
4b
3a
2a
3b
2b
1a
1b
well
fault zone
fault reactivation
Time steps, yrs
b
Surface uplift above the injection zone, cm
c
Fault slip, cm
d
Effective shear strain increment

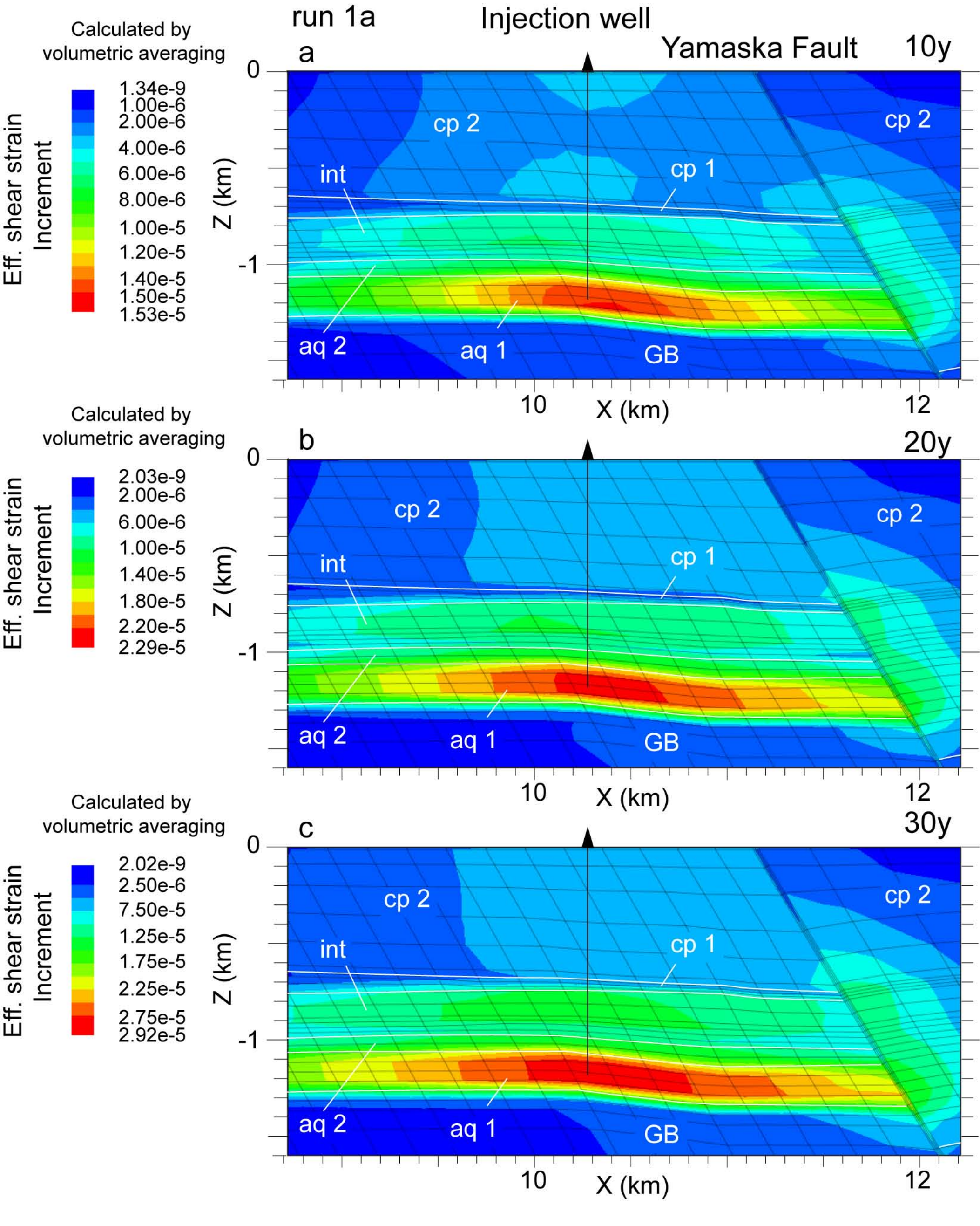

run 1a
Injection well
Yamaska Fault
a
10y
b
20y
c
30y
Calculated by volumetric averaging
Eff. shear strain Increment
1.34e-9
1.00e-6
2.00e-6
4.00e-6
6.00e-6
8.00e-6
1.00e-5
1.20e-5
1.40e-5
1.50e-5
1.53e-5
2.03e-9
2.00e-6
6.00e-6
1.00e-5
1.40e-5
1.80e-5
2.20e-5
2.29e-5
2.02e-9
2.50e-6
7.50e-5
1.25e-5
1.75e-5
2.25e-5
2.75e-5
2.92e-5
cp 2
cp 1
int
aq 2
aq 1
GB
Z (km)
0
-1
X (km)
10
12

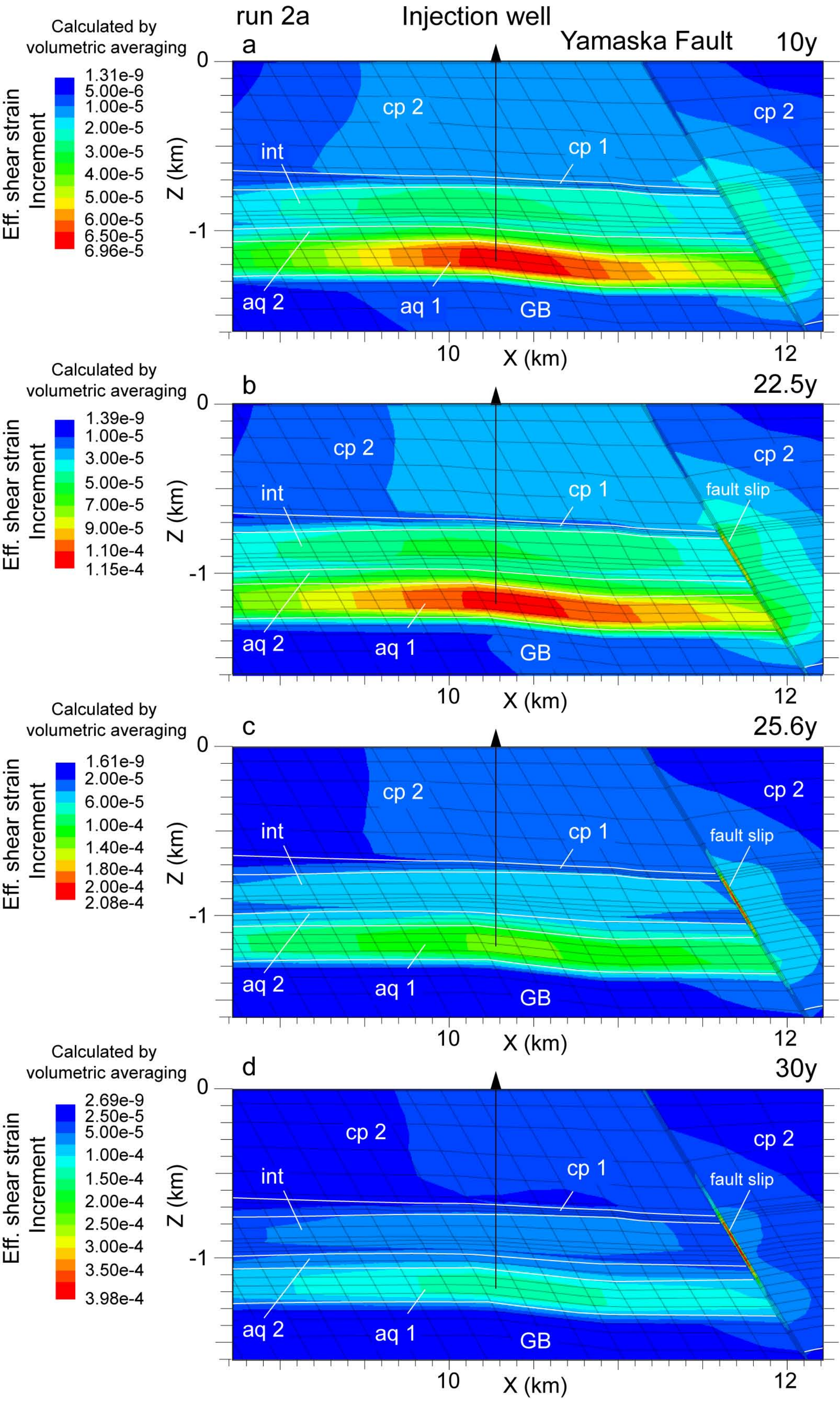

run 2a
Injection well
Yamaska Fault
a
10y
Calculated by volumetric averaging
Eff. shear strain Increment
1.31e-9
5.00e-6
1.00e-5
2.00e-5
3.00e-5
4.00e-5
5.00e-5
6.00e-5
6.50e-5
6.96e-5
Z (km)
0
-1
cp 2
cp 1
int
aq 2
aq 1
GB
X (km)
10
12
b
22.5y
Calculated by volumetric averaging
Eff. shear strain Increment
1.39e-9
1.00e-5
3.00e-5
5.00e-5
7.00e-5
9.00e-5
1.10e-4
1.15e-4
fault slip
c
25.6y
Calculated by volumetric averaging
Eff. shear strain Increment
1.61e-9
2.00e-5
6.00e-5
1.00e-4
1.40e-4
1.80e-4
2.00e-4
2.08e-4
d
30y
Calculated by volumetric averaging
Eff. shear strain Increment
2.69e-9
2.50e-5
5.00e-5
1.00e-4
1.50e-4
2.00e-4
2.50e-4
3.00e-4
3.50e-4
3.98e-4

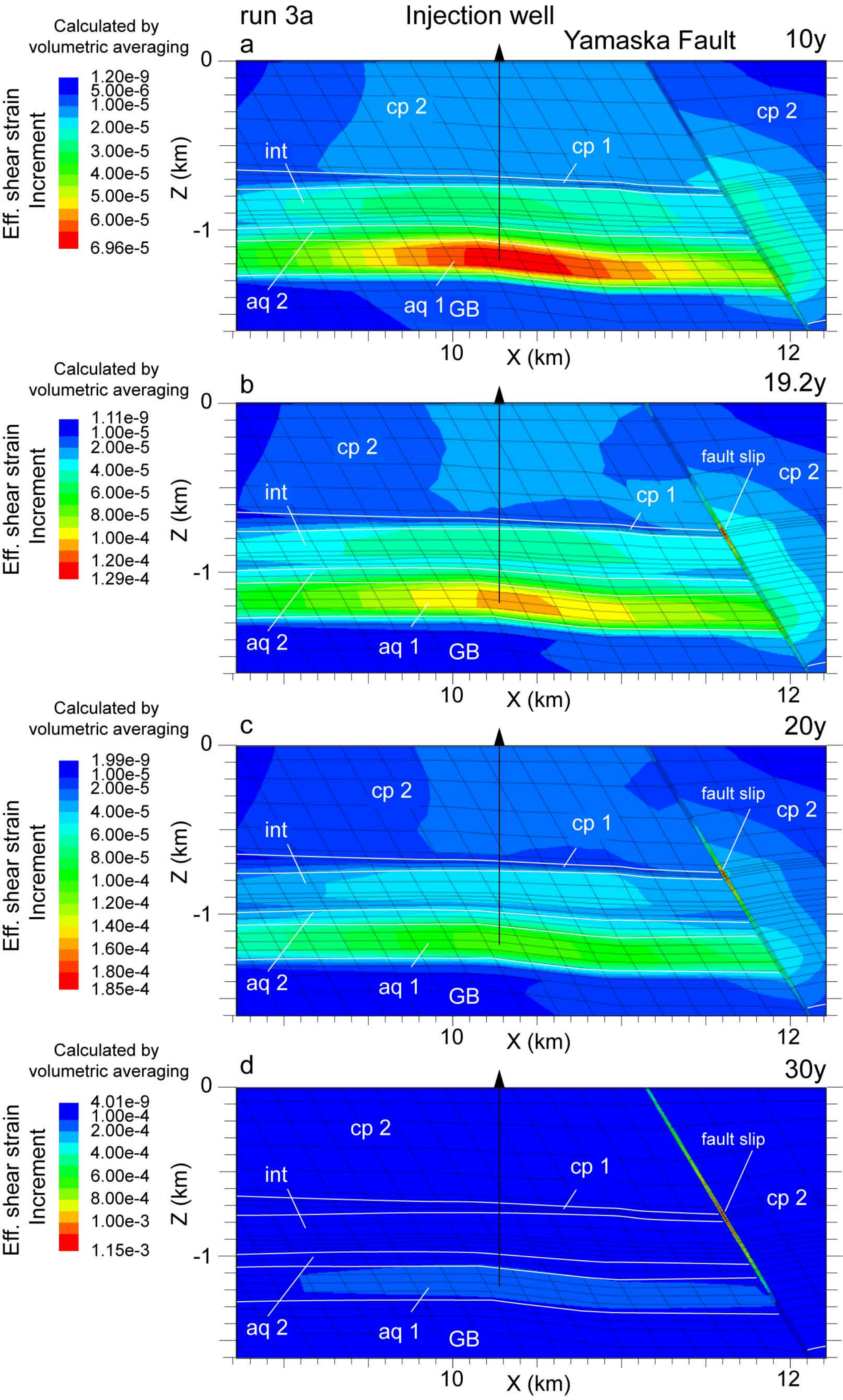

run 3a
Injection well
Yamaska Fault
a
10y
b
19.2y
c
20y
d
30y
Calculated by volumetric averaging
Eff. shear strain Increment
1.20e-9
5.00e-6
1.00e-5
2.00e-5
3.00e-5
4.00e-5
5.00e-5
6.00e-5
6.96e-5
1.11e-9
1.00e-5
2.00e-5
4.00e-5
6.00e-5
8.00e-5
1.00e-4
1.20e-4
1.29e-4
1.99e-9
1.00e-5
2.00e-5
4.00e-5
6.00e-5
8.00e-5
1.00e-4
1.20e-4
1.40e-4
1.60e-4
1.80e-4
1.85e-4
4.01e-9
1.00e-4
2.00e-4
4.00e-4
6.00e-4
8.00e-4
1.00e-3
1.15e-3
Z (km)
0
-1
X (km)
10
12
cp 2
cp 1
int
aq 2
aq 1
GB
fault slip

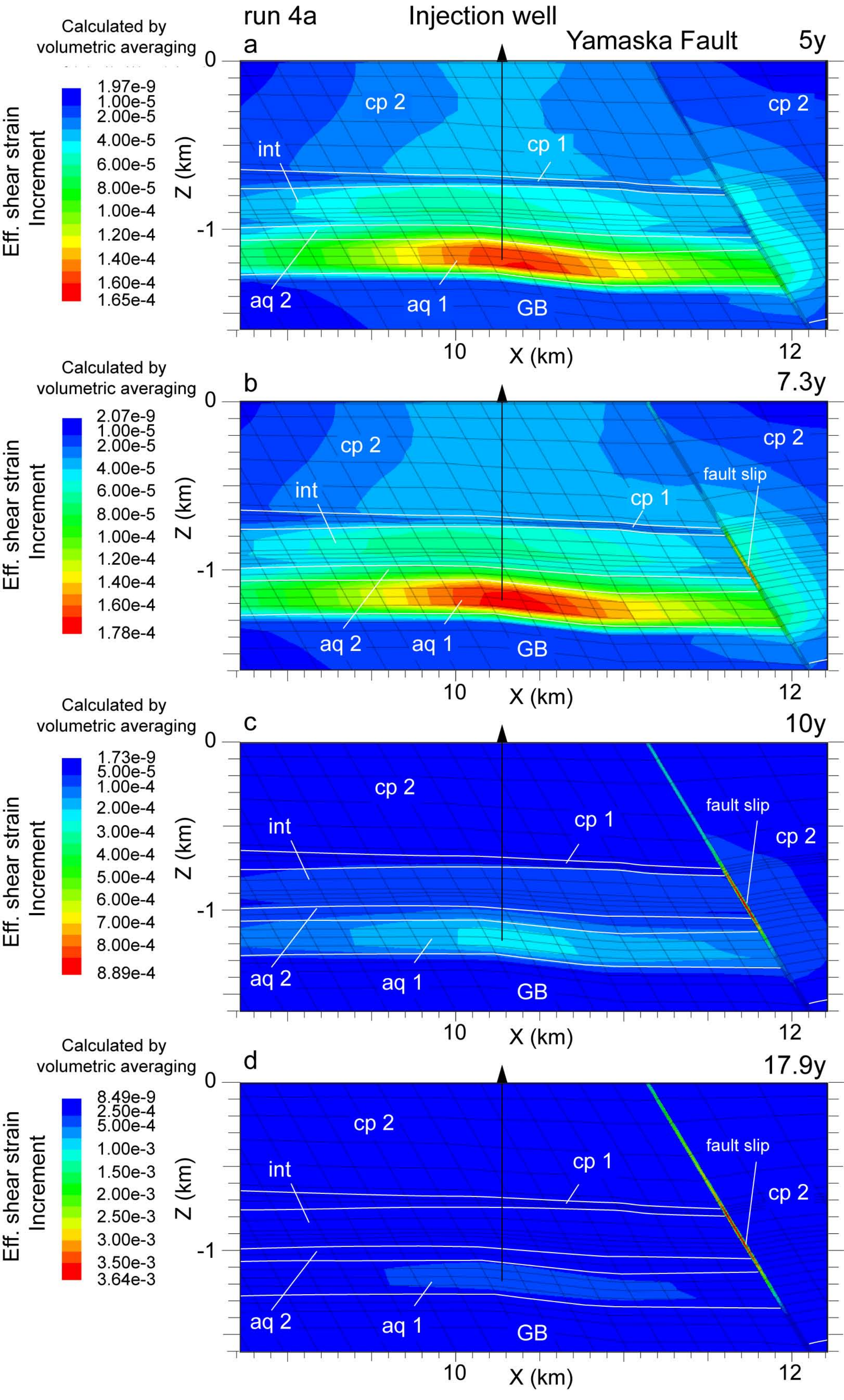

run 4a
Injection well
Yamaska Fault
a
5y
b
7.3y
c
10y
d
17.9y
Calculated by volumetric averaging
Eff. shear strain Increment
1.97e-9
1.00e-5
2.00e-5
4.00e-5
6.00e-5
8.00e-5
1.00e-4
1.20e-4
1.40e-4
1.60e-4
1.65e-4
2.07e-9
1.78e-4
1.73e-9
5.00e-5
1.00e-4
2.00e-4
3.00e-4
4.00e-4
5.00e-4
6.00e-4
7.00e-4
8.00e-4
8.89e-4
8.49e-9
2.50e-4
5.00e-4
1.00e-3
1.50e-3
2.00e-3
2.50e-3
3.00e-3
3.50e-3
3.64e-3
Z (km)
0
-1
X (km)
10
12
cp 2
cp 1
int
aq 2
aq 1
GB
fault slip

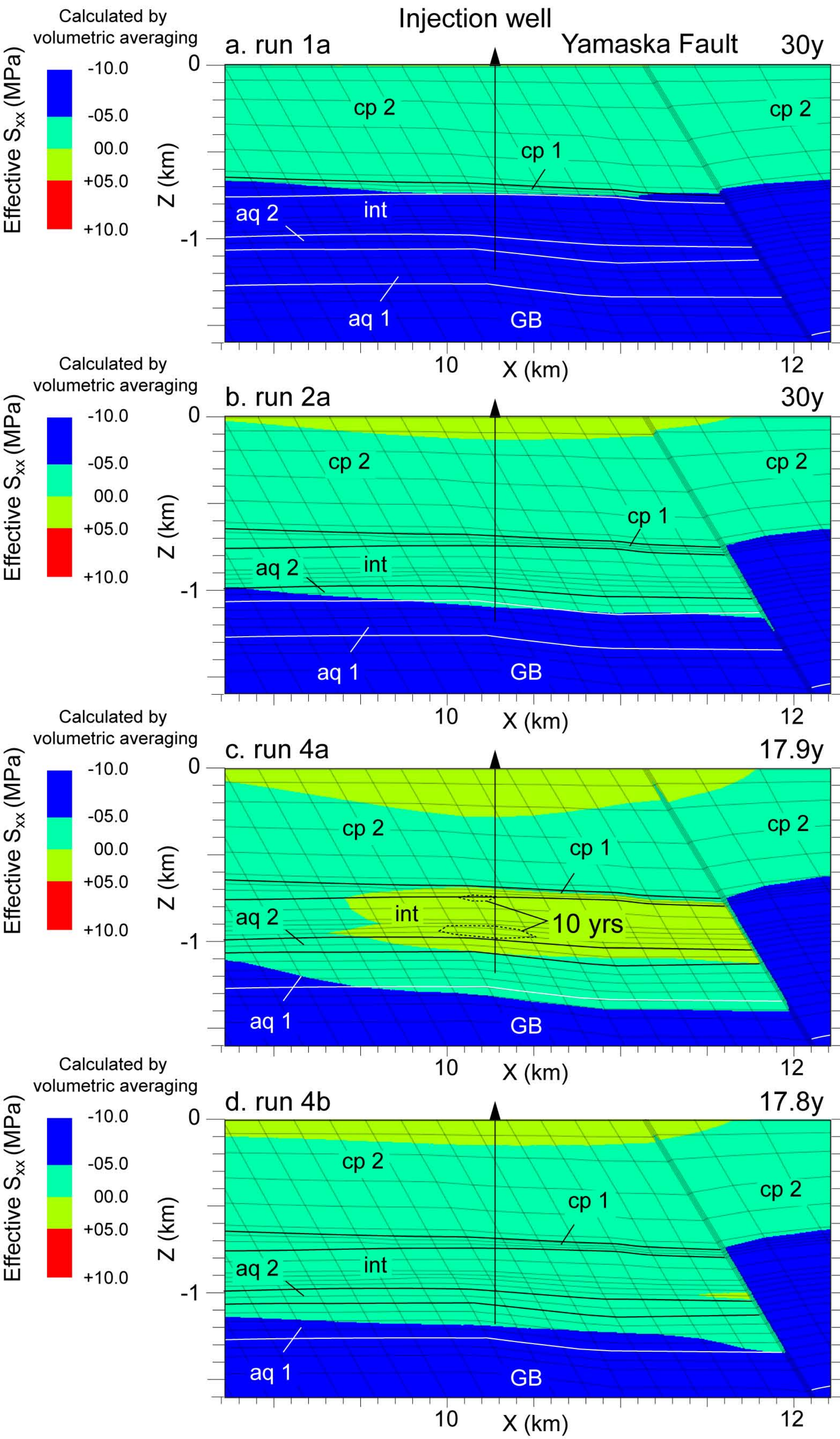

Injection well
Yamaska Fault
Calculated by volumetric averaging
Effective S_{xx} (MPa)
-10.0
-05.0
00.0
+05.0
+10.0
a. run 1a
30y
b. run 2a
30y
c. run 4a
17.9y
d. run 4b
17.8y
Z (km)
X (km)
0
-1
10
12
cp 2
cp 1
int
aq 2
aq 1
GB
10 yrs

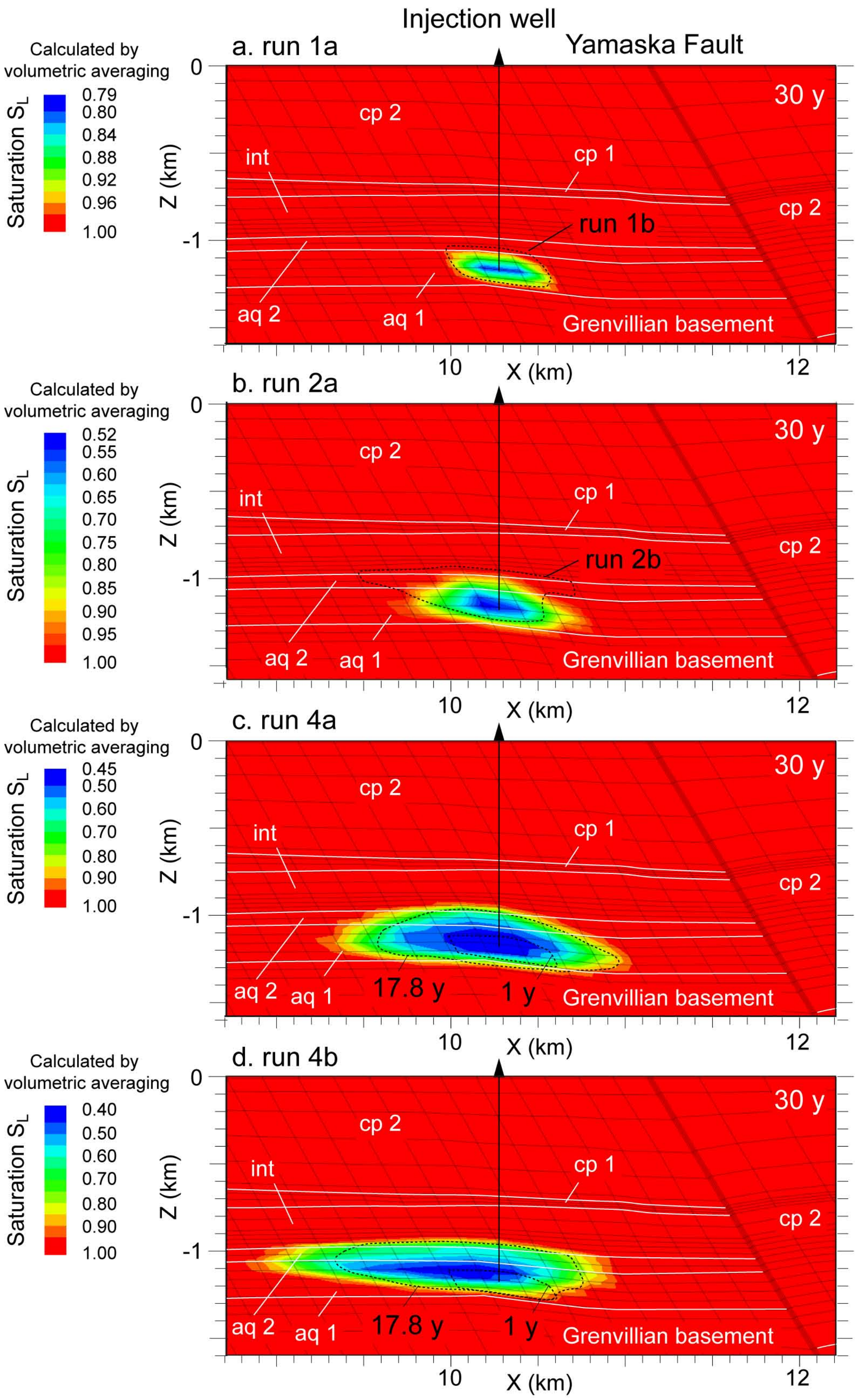

Injection well
Yamaska Fault
a. run 1a
b. run 2a
c. run 4a
d. run 4b
Calculated by volumetric averaging
Saturation S_L
0.79
0.80
0.84
0.88
0.92
0.96
1.00
0.52
0.55
0.60
0.65
0.70
0.75
0.80
0.85
0.90
0.95
1.00
0.45
0.50
0.60
0.70
0.80
0.90
1.00
0.40
0.50
0.60
0.70
0.80
0.90
1.00
Z (km)
0
-1
X (km)
10
12
30 y
cp 2
cp 1
int
aq 2
aq 1
run 1b
run 2b
17.8 y
1 y
Grenvillian basement

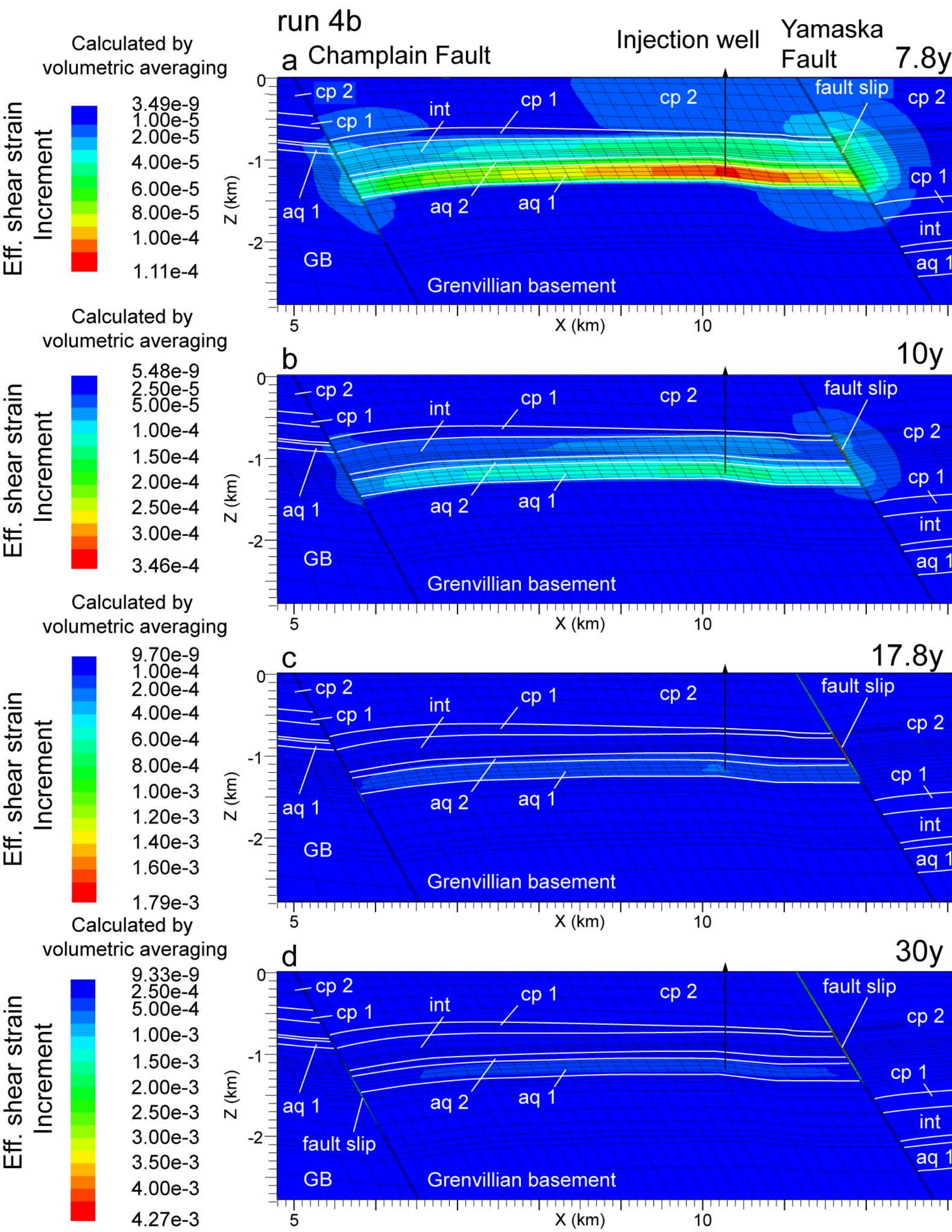

run 4b
Injection well
Yamaska Fault
Champlain Fault
a
7.8y
Calculated by volumetric averaging
Eff. shear strain Increment
3.49e-9
1.00e-5
2.00e-5
4.00e-5
6.00e-5
8.00e-5
1.00e-4
1.11e-4
b
10y
5.48e-9
2.50e-5
5.00e-5
1.00e-4
1.50e-4
2.00e-4
2.50e-4
3.00e-4
3.46e-4
c
17.8y
9.70e-9
1.00e-4
2.00e-4
4.00e-4
6.00e-4
8.00e-4
1.00e-3
1.20e-3
1.40e-3
1.60e-3
1.79e-3
d
30y
9.33e-9
2.50e-4
5.00e-4
1.00e-3
1.50e-3
2.00e-3
2.50e-3
3.00e-3
3.50e-3
4.00e-3
4.27e-3
cp 2
cp 1
int
aq 1
aq 2
GB
Grenvillian basement
fault slip
Z (km)
X (km)

Table 1. Main representative properties of Lower Paleozoic sedimentary units in the Becancour area.

Model	Base	Aquifer 1	Aquifer 2	Intermediate units			Caprock 1	Caprock 2	Fault zone
Property	Grenvillian Basement	Covey Hill Fm	Cairnside Fm	Theresa Fm	Beauharnois Fm	Trenton-Black River-Chazy Gps	Utica Shale	Lorraine Gp	Rock fill/Joint
Lithology	granite	sandstone	sandstone	sandstone	dolomite	limestone	Ca shale	siltstone	Ca shale
Thickness in injection well (m)		195	90	40	34	153	47	694	10 [b]
Netpay thickness in injection well (m)		188	63	4	0	0,5			
Young's modulus, E (GPa)	60	27,56	43,69	53,97	49,28	49,28	42,28	28,71	42,28
Poisson's ratio, ν (-)	0,25	0,022	0,26	0,29	0,23	0,23	0,29	0,32	0,29
Bulk modulus, K (GPa)		16,35	29,84	42,84	30,88	30,88	33,38	26,58	
Shear modulus, G (GPa)		11,30	17,39	20,92	19,97	19,97	16,30	10,87	
Lame's constant λ, (GPa)		8,81	18,25	28,89	17,57	17,57	22,51	19,33	
Rock density, ρ_s (kg/m^3)	2665	2583	2593	2670	2754	2695	2665	2571	2665
Biot's coefficient, α (-)	1	1	1	1	1	1	1	1	
Friction angle, φ (°)									25
Dilation angle, ψ (°)									0
Cohesion, Pa									5E+05
Porosity, ϕ (-)	0,07	0,06	0,04	0,05	0,07	0,09	0,07	0,05	0,07
Matrix permeability, k_m (m^2)		2,6E-16	1,1E-16	1,2E-16	2,3E-16	1,6E-16	1E-18	1E-18	
Rock mass permeability[a], k_1 (m^2)=10k_m	1E-18	2,6E-15	1,56E-15	1,2E-16	2,3E-16	1,6E-16	1E-18	1E-18	1e-18 or 1e-16
Rock mass permeability[a], k_2 (m^2)=100k_m	1E-18	2,6E-14	1,56E-14	1,2E-16	2,3E-16	1,6E-16	1E-18	1E-18	
Salinity (g/l)	n/a	109	242	157	150	179	n/a	n/a	n/a
Residual gas (CO_2) saturation (-)	0,214	0,262	0,214	0,214	0,214	0,214	0,214	0,214	0,214
Residual liquid saturation (-)	0,33	0,273	0,33	0,33	0,33	0,33	0,33	0,33	0,33
Saturated liquid saturation (-)	1	1	1	1	1	1	1	1	1
Entry pressure P_0 (kPa)	40,00	44,10	40,00	40,00	40,00	40,00	40,00	40,00	40,00
Exponent m (-)	0,55	0,5582	0,621	0,55	0,55	0,55	0,55	0,55	0,55
α (1/Pa)	2,00E-05	2,268E-05	2,00E-05	2,00E-05	2,00E-05	2,00E-05	2,00E-05	2,00E-05	2,00E-05
Capillary pressure, max, kPa	200000	200000	200000	200000	200000	200000	200000	200000	200000
Compressibility, 1/Pa	1.861e-9	1.939e-9	3,96E-09	1.861e-9	1.861e-9	1.861e-9	1.861e-9	1.861e-9	1.861e-9

Note: The elastic properties E, ν, porosity and matrix permeability data are obtained from laboratory core analyses; λ, K, and G are calculated from E and ν, after (Zoback, 2010); [a], determined from drill stem tests (Tran Ngoc et al., 2012); k vertical = 0.1 x k horizontal; [b], spacing between joints. Elastic moduli for the Grenvillian basement are taken as an average granite value; for the Trenton-Black River-Chazy Groups - as equal to the Beauharnois Fm; the data on fluid-property parameters (salinity, saturation, capillary pressure, entry pressure and compressibility) are taken from Tran Ngoc et al. (2012).

Table 2. Changes of stress/pressure and temperature with depth in the Becancour area

Average S_{Hmax} orientation	N59°E
Minimum horizontal stress $\Delta S_{hmin} = \Delta S_{xx}$ (MPa/km)	18
Maximum horizontal stress $\Delta S_{Hmax} = \Delta S_{yy}$ (MPa/km)	40
Vertical stress $\Delta S_{v} = \Delta S_{zz}$ (MPa/km)	25,6
Fluid pressure ΔP_{f0} (MPa/km)	12,17
Surface temperature T_0 (°C)	8
Temperature gradient ΔT (°C)	23,5

Table 3. Estimation of seal capacity for the Champlain and the Yamaska Faults using the shale gouge ratio method (Freeman et al., 1998; Yielding et al., 1997)

a. Champlain Fault

Hydrology	Lithological unit	Footwall		Hanging wall		V_{sh}	Fault throw (m)	SGR (%)			
		Z (m)	ΔZ (m)	Z (m)	ΔZ (m)			FW		HW	
Caprock 2	Lorraine Gp	0	484	0	780	0,95			sealing behaviour		permeable?
Caprock 1	Upper Utica Shale	484	152	780	150	0,6	296	95			
Interm. units	Trenton-Black River-Chazy Gps	636	94	930	170	0,14	294	77			
	Beekmantown Gp - Beauharnois Fm	730	50	1100	50	0,1	370	44			
	Beekmantown Gp - Theresa Fm	780	20	1150	50	0,1	370	32		8	
Aquifer 2	Potsdam Gp - Cairnside Fm	800	50	1200	80	0,1	400	28		8	
Aquifer 1	Potsdam Gp - Covey Hill Fm	850	80	1280	200	0,1	430	21		7	
	Grenvillian basement	930	N/A	1480	N/A	N/A	550	11			

b. Yamaska Fault

Hydrology	Lithological unit	Footwall		Hanging wall		V_{sh}	Fault throw (m)	SGR (%)			
		Z (m)	ΔZ (m)	Z (m)	ΔZ (m)			FW		HW	
Caprock 2	Lorraine Gp	0	724	0	1520	0,95			sealing behaviour		
Caprock 1	Upper Utica Shale	724	48	1520	88	0,6	796	95			
	Lower Utica Shale	772	51	1610	83	0,44	838	91			
Intermed. units	Trenton-Black River-Upper Chazy Gps	822	117	1703	148	0,14	881	85		9	permeable?
	Lower Chazy Gp	939	23	1851	34	0,1	912	73			
	Beekmantown Gp - Beauharnois Fm	960	63	1889	109	0,1	929	69			
	Beekmantown Gp - Theresa Fm	1025	72	2011	122	0,1	986	60			
Aquifer 2	Potsdam Gp - Cairnside Fm	1102	107	2134	171	0,1	1032	52		7	
Aquifer 1	Potsdam Gp - Covey Hill Fm	1215	291	2315	404	0,1	1100	40		7	
	Grenvillian basement	1503	N/A	2736	N/A	N/A	1233	17			

Note: V_{sh}, volume of shale estimated from natural radioactivity (gamma ray) well log data; Z, depth of formation tops estimated for the Yamaska Fault as an average value from the 3D geological model of the Becancour area (Claprood et al., 2012) and for the Champlain Fault from correlation of regional well data and basement top (Fig. 3). FW, footwall, HW, hanging wall.

Table 4. Initial parameters used in numerical simulations

Series #	run #	Injection rate	Fault permeability	Reservoir permeability			Corresponding 3D injection rate (r=3.5 km)	
				Aquifer 1 CH	Aquifer 2 Ca			
		kg/s	m^2	m^2	m^2		kg/s	Mt/yr.
Series 1	1a	0,06	1E-18	2,60E-15	1,56E-15	k_1 =10 k_m	4,5	0,15
	2a	0,3	1E-18				23	0,8
	3a		1E-16					
	4a	1	1E-18				75	2,5
Series 2	1b	0,06	1E-18	2,60E-14	1,56E-14	k_2 =100 k_m	4,5	0,15
	2b	0,3	1E-18				23	0,8
	3b		1E-16					
	4b	1	1E-18				75	2,5

Note: CH, Covey Hill Fm; Ca, Cairnside Fm; k_1, k_2, rock mass permeability; k_m, matrix permeability (see Table 1).

Table 5. Resulting variations in fluid pressure build-up (ΔP_f), effective shear strain increment ($\Delta\gamma$), surface uplift (h), length of reactivated fault segment (L), fault shear slip (d), effective minimum horizontal stress (S_{xx}*) and CO_2 plume width (W) observed in numerical simulations 1a-4a of series 1 (k_1 = 10k_m) for different injection rates (IR) and fault permeability (k_f).

	Initial parameters			Resulting data										
run #	IR	k_f	time step	$\Delta P_{f} = P_{f} - P_{f0}$		$\Delta\gamma$		h	Yamaska Fault			S_{xx}*		W
				well	YF zone	well	YF zone		reactivated segment		d			
	kg/s	m^2	yrs	MPa	MPa			cm	L (m)	FW unit	cm	MPa	unit	km
1a	0,06	1E-18	10	1,04	0,7	1,55E-05	1,10E-05	0,8						
			20	1,44	1,3	2,30E-05	2,00E-05	1,5						
			30	1,8	1,7	2,90E-05	2,50E-05	2,05	no			negative		0,5
2a	0,3	1E-18	10	4,5	3,25	7,00E-05	5,50E-05	4						
			22,5	7,1	6,5	1,20E-04	1,20E-04	7	300	th-Tr	0,5			
			25,6	7,6	7	1,40E-04	2,07E-04	8	400	Ca-Tr	0,5			
			30	8,4	7,5	1,50E-04	3,99E-04	9	550	CH-Ut	1	negative		0,9
3a	0,3	1E-16	10	4,5	3,25	6,99E-05	5,00E-05	4						
			18,2	6,26	5,5	1,02E-04	1,02E-04	6,5	60	Ut	0,5			
			19,2	6,4	5,5	1,10E-04	1,29E-04	6,5	180	Tr-Ut	0,5			
			20	6,6	6	1,10E-04	1,85E-04	6,5	500	th-Lor	0,5			
			23,7	7,3	6,5	1,50E-04	4,70E-04	7,5	830	Ca-Lor	1,5			
			30	8,3	7,5	2,00E-04	1,40E-03	9	1300	CH-Lor	4	negative		0,9
4a	1	1E-18	5	11	5	1,60E-04	1,10E-04	8						
			7,3	11,8	7	1,80E-04	1,80E-04	9	330	Ca-Tr	1			
			10	13,9	10	2,50E-04	9,40E-04	12	450	Ca-Ut	2	(+2)	th, Tr	
			17,9	18,8	16	2,80E-04	5,20E-03	20	700	Ca-Lor	12			1,3
			30	24,9	24	3,50E-04	1,00E-02	27,5	1400	CH-Lor	17	(+4)	Ca-Ut	1,7

Note: YF, Yamaska Fault; FW unit, footwall unit: CH, Covey Hill Fm; Ca, Cairnside Fm; th, Theresa Fm; Tr, Trenton Gp; Ut, Utica Shale; Lor, Lorraine Gp. See Table 4 for the rock mass k_1 and matrix k_m permeability of the reservoir units.

Table 6. Resulting variations in fluid pressure build-up (ΔP_f), effective shear strain increment ($\Delta\gamma$), surface uplift (h), length of reactivated fault segment (L), fault shear slip (d), effective minimum horizontal stress (S_{xx}*) and CO_2 plume width (W) observed in numerical simulations 1b-4b of series 2 (k_2 = 100k_m) for different injection rates (IR) and fault permeability (k_f).

	Initial parameters			Resulting data										
run #	IR	k_f	time step	$\Delta P_f = P_f - P_{f0}$		$\Delta\gamma$		h	Yamaska Fault			S_{xx}*		W
				well	YF zone	well	YF zone		reactivated segment		d			
	kg/s	m^2	yrs	MPa	MPa			cm	L (m)	FW unit	cm	MPa	unit	km
			10	0,51	0,5	8,80E-06	7,50E-06	0,55						
1b	0,06	1E-18	20	0,87	0,87	1,50E-05	1,30E-05	0,9						
			30	1,21	1,2	2,13E-05	1,80E-05	1,4	no			negative		0,5
			10	2,5	2,4	4,10E-05	3,50E-05	2,5						
2b	0,3	1E-18	20	4,25	4,25	7,20E-05	6,00E-05	4,5						
			30	5,8	5,8	9,90E-05	8,50E-05	6,5	no			negative		1,2
			10	2,47	2,4	4,10E-05	3,50E-05	2,5						
			20	4,2	4	7,10E-05	6,00E-05	4,5						
3b	0,3	1E-16	27,5	5,4	5,4	9,40E-05	9,40E-05	6	60	Ut	0,5			
			28,5	5,5	5,5	1,00E-04	1,14E-04	6,5	180	Tr-Ut	0,5			
			29,5	5,6	5,5	1,00E-04	1,54E-04	6,5	500	th-Lor	0,5			
			30	5,7	5,5	1,00E-04	1,83E-04	6,5	700	Ca-Lor	0,5	negative		1,2
			5	5,6	5,6	9,50E-05	8,00E-05	5,5						
			7,8	6,6	6,6	1,11E-04	1,10E-04	7	330	Ca-Tr	0,5			
4b	1	1E-18	10	7,8	7,8	1,50E-04	3,47E-04	8,5	450	Ca-Ut	0,5			
			17,8	11,7	11,7	2,00E-04	1,79E-03	13,7	800	Ca-Lor	5	(+0,4)	th	
			20	12,75	12,75	2,00E-04	2,90E-03	15	1200	CH-Lor	5			
			30	17	17	2,50E-04	6,00E-03	21	500[a]/1400	GB[a]/CH-Lor	10	(+2,8)	th-Ut	2

Note: YF, Yamaska Fault; [a], reactivation of the Champlain Fault; FW unit, footwall unit: GB, Grenvillian basement; CH, Covey Hill Fm; Ca, Cairnside Fm; th, Theresa Fm; Tr, Trenton Gp; Ut, Utica Shale; Lor, Lorraine Gp. See Table 4 for the rock mass k_2 and matrix k_m permeability of the reservoir units.

Appendix. Name and location of wells in the St. Lawrence Lowlands cited in present study. See Fig. 2 for well location.

NN	Well no.	Well Name	Year	Location (UTM NAD83 z18)		Elevation	End depth
				X	Y	mKB	mKB
1	A027	Canadian Seaboard. Sainte-Angèle No 1	1933	693564,84	5132519,55	25,60	1603,25
2	A156	Husky, Gentilly No 1	1971	709333,23	5137234,43	41,75	2612,14
3	A158	Husky Bruyères No 1	1971	692730,38	5133160,72	34,53	1390,50
4	A175	SOQUIP et al., Les Saules No 1	1975	779535,52	5191473,39	49,14	975,66
5	A196	SOQUIP Petrofina Bécancour 1	1981	699140,79	5138042,62	12,85	1228,00
6	A198	SOQUIP Pétrofina, Bécancour No 2	1981	700814,50	5140665,43	11,78	1265,00
7	A223	Intermont. Bécancour No 1	1992	699612,00	5139396,00	11,26	850,70
8	A236	Junex. Bécancour No 2	2002	699874,99	5138967,52	10,10	930,00
9	A239	Junex. Bécancour No 3	2003	699174,51	5139533,47	7,25	935,50
10	A241	Junex. Bécancour No 4	2003	698745,33	5139237,59	8,20	1054,00
11	A242	Junex. Bécancour No 5	2003	700446,31	5140457,08	7,91	981,36
12	A246	Junex. Bécancour No 6	2004	701027,30	5140831,13	8,35	1002,18
13	A247	Junex. Bécancour No 7	2004	698042,90	5136740,50	9,40	1069,23
14	A250	Junex. Bécancour No 8	2006	697878,26	5137501,40	7,20	1048,00
15	A251	Junex, Champlain No 1	2006	699650,95	5143492,47	8,41	958,00
16	A255	Junex, Champlain No 2	2007	697763,02	5144709,86	22,79	930,00
17	A257	Junex Saint-Augustin-de-Desmaures No 1	2008	769981,51	5184176,63	74,43	837,00
18	A262	Junex, Bécancour No 8	2008	700265,33	5134581,73	34,65	1902,71
19	A265	Canadian Forest Oil, Champlain No 1-H	2008	699572,42	5143424,57	7,85	1482,00